Effects of the diurnal cycle in solar radiation on the tropical Indian Ocean mixed layer variability during wintertime Madden-Julian Oscillations

Yuanlong Li,[1] Weiqing Han,[1] Toshiaki Shinoda,[2] Chunzai Wang,[3] Ren-Chieh Lien,[4] James N. Moum,[5] and Jih-Wang Wang[6]

[1] The effects of solar radiation diurnal cycle on intraseasonal mixed layer variability in the tropical Indian Ocean during boreal wintertime Madden-Julian Oscillation (MJO) events are examined using the HYbrid Coordinate Ocean Model. Two parallel experiments, the main run and the experimental run, are performed for the period of 2005–2011 with daily atmospheric forcing except that an idealized hourly shortwave radiation diurnal cycle is included in the main run. The results show that the diurnal cycle of solar radiation generally warms the Indian Ocean sea surface temperature (SST) north of 10°S, particularly during the calm phase of the MJO when sea surface wind is weak, mixed layer is thin, and the SST diurnal cycle amplitude ($dSST$) is large. The diurnal cycle enhances the MJO-forced intraseasonal SST variability by about 20% in key regions like the Seychelles-Chagos Thermocline Ridge (SCTR; 55°–70°E, 12°–4°S) and the central equatorial Indian Ocean (CEIO; 65°–95°E, 3°S–3°N) primarily through nonlinear rectification. The model also well reproduced the upper-ocean variations monitored by the CINDY/DYNAMO field campaign between September-November 2011. During this period, $dSST$ reaches 0.7°C in the CEIO region, and intraseasonal SST variability is significantly amplified. In the SCTR region where mean easterly winds are strong during this period, diurnal SST variation and its impact on intraseasonal ocean variability are much weaker. In both regions, the diurnal cycle also has a large impact on the upward surface turbulent heat flux Q_T and induces diurnal variation of Q_T with a peak-to-peak difference of $O(10 \text{ W m}^{-2})$.

1. Introduction

1.1. MJO and Indian Ocean Intraseasonal Variability

[2] As the major mode of intraseasonal variability of the tropical atmosphere, the Madden-Julian Oscillation (MJO) [*Madden and Julian*, 1971] has a profound climatic impact at a global scale [e.g., *Zhang*, 2005]. The MJO is characterized by large-scale fluctuations of atmospheric deep convection and low-level winds at periods of 20–90 days and propagates eastward at a mean speed of 5 m s^{-1} over warm areas of the tropical Indian and Pacific Oceans. At the lowest order, the MJO was considered to be an intrinsic convection-wind coupling mode of the tropical atmosphere [e.g., *Knutson and Weickmann*, 1987; *Wang and Rui*, 1990; *Zhang and Dong*, 2004]. Recently, the role of air-sea interaction in the MJO dynamics is receiving increasing interest. As a major source of heat and moisture, the mixed layer of the tropical Indian Ocean (TIO) plays an important role in the initiation and development of the MJO convection. Modeling studies demonstrate that including air-sea coupling on intraseasonal timescale can improve the simulation [e.g., *Wang and Xie*, 1998; *Waliser et al.*, 1999; *Woolnough et al.*, 2001; *Inness and Slingo*, 2003; *Inness et al.*, 2003; *Sperber et al.*, 2005; *Zhang et al.*, 2006; *Watterson and Syktus*, 2007; *Yang et al.*, 2012] and forecast [e.g., *Waliser*, 2005; *Woolnough et al.*, 2007] of the MJO behaviors. However, because the MJO-related air-sea coupling processes are not well understood, realistically representing the MJO is still a challenging task for the state-of-

[1]Department of Atmospheric and Oceanic Sciences, University of Colorado, Boulder, Colorado, USA.
[2]Department of Physical & Environmental Sciences, Texas A&M University, Corpus Christi, Texas, USA.
[3]NOAA/Atlantic Oceanographic and Meteorological Laboratory, Miami, Florida, USA.
[4]Applied Physics Laboratory, University of Washington, Seattle, Washington, USA.
[5]College of Earth, Ocean and Atmospheric Sciences, Oregon State University, Corvallis, Oregon, USA.
[6]Cooperative Institute for Research in Environmental Sciences, Boulder, Colorado, USA.

Corresponding author: Y. Li, Department of Atmospheric and Oceanic Sciences, University of Colorado, Campus Box 311, Boulder, CO 80309, USA. (yuanlong.li@colorado.edu)

the-art climate models [e.g., *Lin et al.*, 2006; *Zhang et al.*, 2006; *Lau et al.*, 2012; *Sato et al.*, 2009; *Xavier*, 2012]. Given that the tropical ocean affects the atmosphere through mainly sea surface temperature (SST), investigating the TIO intraseasonal SST variability and associated upper-ocean processes will help improve our understanding of air-sea interaction processes on intraseasonal timescale.

[3] With the advent of satellite microwave SST products, strong intraseasonal SST signals with 1–2°C magnitudes have been detected in the TIO [e.g., *Harrison and Vecchi*, 2001; *Sengupta et al.*, 2001; *Duvel et al.*, 2004; *Saji et al.*, 2006; *Duvel and Vialard*, 2007]. During boreal winter, the strong 20–90 day SST variability in the southern TIO, particularly in the Seychelles-Chagos thermocline ridge (SCTR) region [*Hermes and Reason*, 2008], is shown to be associated with wintertime MJO events [e.g., *Waliser et al.*, 2003; *Duvel et al.*, 2004; *Saji et al.*, 2006; *Duvel and Vialard*, 2007; *Han et al.*, 2007; *Vinayachandran and Saji*, 2008; *Izumo et al.*, 2010; *Lloyd and Vecchi*, 2010; *Jayakumar et al.*, 2011; *Jayakumar and Gnanaseelan*, 2012]. During boreal winter, SST in the SCTR is high, but the thermocline and mixed layer depth (MLD) are shallow due to the Ekman upwelling induced by the large-scale wind stress curl [*McCreary et al.*, 1993; *Xie et al.*, 2002; *Schott et al.*, 2009]. These mean conditions favor large-amplitude SST response to intraseasonal radiation and wind changes associated with the MJO. In addition, the SCTR is located at the western edge of the intertropical convergence zone (ITCZ) and close to the initiation area of most strong wintertime MJO events [*Wheeler and Hendon*, 2004; *Zhang*, 2005; *Zhao et al.*, 2013]. In this region, relatively small changes in SST may induce significant perturbations in atmospheric convection and thus may have a profound impact on weather and climate [*Xie et al.*, 2002; *Vialard et al.*, 2009]. The feedbacks of SST anomalies (SSTA) onto the atmosphere are believed to be essential in organizing the large-scale convection and facilitating the eastward propagation of the MJO [e.g., *Flatau et al.*, 1997; *Woolnough et al.*, 2001, 2007; *Bellenger et al.*, 2009; *Webber et al.*, 2012], and are also important in determining their phase, time scale, spatial structure, and propagation paths [e.g., *Saji et al.*, 2006; *Izumo et al.*, 2010].

[4] The mechanism that controls intraseasonal SST variability is, however, still under debate. While some studies emphasize the importance of wind forcing and ocean dynamics [*Harrison and Vecchi*, 2001; *Saji et al.*, 2006; *Han et al.*, 2007; *Vinayachandran and Saji*, 2008], others show the significant effects of shortwave radiation [*Duvel et al.*, 2004; *Duvel and Vialard*, 2007, *Vialard et al.*, 2008; *Zhang et al.*, 2010; *Jayakumar et al.*, 2011; *Jayakumar and Gnanaseelan*, 2012]. To improve our understanding of the intraseasonal TIO SST variability and its feedbacks to the MJO convection, further investigation is needed to address other involved processes, such as the diurnal cycle's effects.

1.2. Diurnal Cycle of SST

[5] Due to the large day/night difference in solar radiation, SST exhibits large-amplitude diurnal variation [*Sverdrup et al.*, 1942]. Since the 1960s, large diurnal warming (*dSST*) with magnitude > 1°C has been frequently detected by in situ and satellite observations throughout the world's oceans [e.g., *Stommel et al.*, 1969; *Halpern and*

Reed, 1976; *Deschamps and Frouin*, 1984; *Price et al.*, 1986; *Stramma et al.*, 1986]. In the tropics, diurnal warming can reach as large as 2–3°C under clear-sky, low-wind condition [e.g., *Flament et al.*, 1994; *Webster et al.*, 1996; *Soloviev and Lukas*, 1997; *Stuart-Menteth et al.*, 2003; *Kawai and Wada*, 2007; *Kennedy et al.*, 2007; *Gille*, 2012]. During the calm (suppressed) phase of the MJO, such condition is satisfied in the TIO. The large daytime ocean warming at the calm phase induces an increase of the net surface heat flux toward the atmosphere by > 50 W m^{-2} [*Fairall et al.*, 1996], which can significantly alter the vertical distributions of heat, moisture, and buoyance of the atmosphere, and thereby influence the formation and development of the MJO convection system [*Webster et al.*, 1996; *Woolnough et al.*, 2000, 2001; *Yang and Slingo*, 2001; *Slingo et al.*, 2003; *Dai and Trenberth*, 2004; *Bellenger et al.*, 2010].

[6] Except for a direct feedback to the atmosphere, the diurnal ocean variation can also impact intraseasonal SST variability associated with the MJO. Recent modeling studies showed that resolving the diurnal cycle of solar radiation forcing in ocean models amplifies the intraseasonal SST variability by about 20%–30% in the tropical oceans [*Shinoda and Hendon*, 1998; *McCreary et al.*, 2001; *Bernie et al.*, 2005, 2007; *Shinoda*, 2005; *Guemas et al.*, 2011] via nonlinear effect [*Shinoda and Hendon*, 1998; *Bernie et al.*, 2005; *Shinoda*, 2005]. During daytime, strong short-wave heating Q_{SW} stabilizes the upper ocean and thins the mixed layer. As a result, a large amount of Q_{SW} is absorbed by the upper few meters of the ocean, which significantly increases the SST. At night, cooling destabilizes the upper ocean and erodes the diurnal warm layer created during daytime. However, further cooling of SST is usually very small because it requires a lot of energy to entrain deeper water into the mixed layer [*Shinoda*, 2005]. As a result, the daily mean SST is higher with the diurnal cycle forcing of Q_{SW}. This effect primarily occurs during the calm phase of the MJO when high insolation and low winds produce a thin mixed layer and a strong SST diurnal cycle, which can therefore enhance the intraseasonal SST variability associated with the MJO. Such effect may also contribute to the underestimation of the MJO signals in coupled models that do not resolve the diurnal cycle [e.g., *Inness and Slingo*, 2003; *Zhang et al.*, 2006].

[7] Modeling studies also suggest that the diurnal cycle of solar radiation can modify the mean state of the tropical oceans [e.g., *Schiller and Godfrey*, 2003; *Bernie et al.*, 2007, 2008] and improve the simulation of large-scale tropical climate variability such as the MJO [*Woolnough et al.*, 2007; *Bernie et al.*, 2008; *Oh et al.*, 2012], Indian Monsoon [*Terray et al.*, 2012], and El Niño-Southern Oscillation (ENSO) [*Danabasoglu et al.*, 2006; *Masson et al.*, 2012]. These findings have greatly improved our understanding of the role of the diurnal cycle in the tropical climate system. Among the existing studies, however, investigations of diurnal ocean variation are mainly for the western Pacific warm pool region [*Shinoda and Hendon*, 1998; *Bernie et al.*, 2005; *Shinoda*, 2005] or the Atlantic Ocean [*Pimentel et al.*, 2008; *Guemas et al.*, 2011], whereas coupled model studies focus primarily on the general effects of diurnal coupling on the mean structure and low-frequency variability of the climate [*Danabasoglu*

et al., 2006; *Bernie et al.*, 2008; *Noh et al.*, 2011; *Oh et al.*, 2012; *Masson et al.*, 2012; *Guemas et al.*, 2013]. In the present study, we examine the effects of diurnal cycle on the intraseasonal SST variability in the TIO region where many winter MJO events originate, which has not yet been sufficiently explored by previous researches.

1.3. CINDY/DYNAMO Field Campaign

[8] DYNAMO (Dynamics of the MJO; http://www.eol.ucar.edu/projects/dynamo/) is a U.S. program that aims to advance our understanding of processes key to MJO initiation over the Indian Ocean and therefore improve the MJO simulation and prediction. As the first step, the DYNAMO joined the international field program of CINDY (Cooperative Indian Ocean Experiment on Intraseasonal Variability) in 2011 to collect in situ observations [*Zhang et al.*, 2013]. The CINDY/DYNAMO field campaign [*Yoneyama et al.*, 2013] took place in the central equatorial Indian Ocean (CEIO) during September 2011–March 2012. These field observations will serve as constraints and validation for modeling studies. Its atmospheric component includes two intensive sounding arrays, a multiple wavelength radar network, a ship/mooring network to measure air-sea fluxes, the marine atmospheric boundary layer, and aircraft operations to measure the atmospheric boundary layer and troposphere property variations. The oceanic component includes an array of surface buoys and conductivity-temperature-depth (CTD) casts from research vessels in the CEIO. During the monitor period, active episodes of large-scale convection associated with wintertime MJOs were observed to propagate eastward across the TIO [*Shinoda et al.*, 2013b]. The synchronous records of oceanic variability during MJO events are used here to validate the model simulations and examine the potentially crucial upper-ocean processes in the MJO initiation.

1.4. Present Research

[9] The present study has two objectives. First, by including the diurnal cycle of solar radiation in the forcing fields of a high-resolution ocean general circulation model (OGCM), we aim to examine the effects of the diurnal cycle on intraseasonal variability of the surface mixed layer in the TIO. Particular attention will be paid to the SCTR and CEIO regions, which are important regions for wintertime MJO initiation and propagation. Second, we specifically investigate how the Q_{SW} diurnal cycle influences intraseasonal oceanic variability and feedbacks to surface heat flux during the CINDY/DYNAMO field campaign. The results are expected to complement our knowledge of air-sea interaction associated with MJO dynamics and hence contribute to the DYNAMO program. The rest of the paper is organized as follows. Section 2 outlines the OGCM configurations and experiment design. Section 3 provides a comprehensive comparison of the model results with available in situ/satellite observations. Section 4 reports our major research findings. Finally, Section 5 provides the summary and discussion.

2. Model and Experiments

2.1. Model Configuration

[10] The OGCM used in this study is the HYbrid Coordinate Ocean Model (HYCOM) version 2.2.18, in which isopycnal, sigma (terrain following), and *z*-level coordinates are combined to optimize the representation of oceanic processes [*Bleck*, 2002; *Halliwell*, 2004; *Wallcraft et al.*, 2009]. In recent researches, HYCOM has been successfully used to investigate a wide range of ocean processes at various timescales in the Indo-Pacific and tropical Atlantic Oceans [e.g., *Han et al.*, 2006, 2007, 2008; *Yuan and Han*, 2006; *Kelly et al.*, 2007; *Kara et al.*, 2008; *Duncan and Han*, 2009; *Metzger et al.*, 2010; *Nyadjro et al.*, 2012; *Shinoda et al.*, 2012; *Wang et al.*, 2012a, 2012b]. In this study, HYCOM is configured to the tropical and subtropical Indo-Pacific basin (30°E–70°W, 40°S–40°N) with a horizontal resolution of 0.25° × 0.25°. Realistic marine bathymetry from the National Geophysical Data Center (NGDC) 2′ digital data are used with 1.5° × 1.5° smoothing. The smoothed bathymetry is carefully checked and compared with the General Bathymetric Chart of the Oceans (GEBCO) [*Smith and Sandwell*, 1997] in the Indonesian Seas to ensure the important passages of the throughflow are well resolved. No-slip conditions are applied along continental boundaries. At the open-ocean boundaries near 40°S and 40°N, 5° sponge layers are applied to relax the model temperature and salinity fields to the World Ocean Atlas 2009 (WOA09) annual climatological values [*Antonov et al.*, 2010; *Locarnini et al.*, 2010].

[11] The model has 35 vertical layers, with 10 layers in the top 11 m to resolve the diurnal warm layer. *Bernie et al.* [2005] suggested that for the K-Profile Parameterization (KPP), the thickness of the uppermost layer is critical in resolving the diurnal SST variation. In our model, the thickness of the uppermost layer is set to be 0.52 m. The thickness gradually increases with depth. In most areas of the open ocean, the mean layer thickness is smaller than 5, 10, and 20 m in the upper 100, 200, and 500 m, respectively. The diffusion/mixing parameters of the model are identical to those used in *Wang et al.* [2012a]. The nonlocal KPP [*Large et al.*, 1994, 1997] mixing scheme is used. Background diffusivity for internal wave mixing is set to 5 × 10⁻⁶ m² s⁻¹ [*Gregg et al.*, 2003], and viscosity is set to be 1 order larger (5 × 10⁻⁵ m² s⁻¹) [*Large et al.*, 1994]. The diapycnal mixing coefficient is $(1 \times 10^{-7} \text{ m}^2 \text{ s}^{-2}) N^{-1}$, where N is the Brunt-Väisälä frequency. Isopycnal diffusivity and viscosity values are parameterized as $u_d \Delta x$, where Δx is the local horizontal mesh size, and u_d is the dissipation velocity. We set $u_d = 1.5 \times 10^{-2}$ m s⁻¹ for Laplacian mixing and 5 × 10⁻³ m s⁻¹ for biharmonic mixing of momentum, and $u_d = 1 \times 10^{-3}$ m s⁻¹ for Laplacian mixing of temperature and salinity. Shortwave radiation Q_{SW} penetration is computed using Jerlov water type I [*Jerlov*, 1976].

2.2. Forcing Fields

[12] The surface forcing fields of HYCOM include 2 m air temperature and humidity, surface net shortwave, and longwave radiation (Q_{SW} and Q_{LW}), precipitation, 10 m wind speed, and wind stress. The turbulent heat flux Q_T, which consists of the latent and sensible heat fluxes, are not treated as external forcing but automatically estimated by the model with wind speed, air temperature, specific humidity, and SST, using the Coupled Ocean-Atmosphere Response Experiment (COARE 3.0) algorithm [*Fairall et al.*, 2003; *Kara et al.*, 2005]. In our experiments, the 2 m air temperature and humidity are adopted from the

European Centre for Medium-Range Weather Forecasts (ECMWF) Reanalysis Interim (ERA-Interim) products [*Dee et al.*, 2011], which have a 0.7° horizontal resolution available for the period of 1989–2011.

[13] For the surface shortwave and longwave radiation, we use the daily, geostationary enhanced 1° product from Clouds and the Earth's Radiant Energy System (CERES) [*Wielicki et al.*, 1996; *Loeb et al.*, 2001] of the National Aeronautics and Space Administration (NASA) for the period of March 2000–November 2011. Given that Q_{SW} is crucial in modeling intraseasonal and diurnal ocean variability, the quality of the CERES product should be validated. Figure 1 compares the CERES Q_{SW} with in situ measurements by the Research Moored Array for African-Asian-Australian Monsoon Analysis and Prediction (RAMA) mooring arrays [*McPhaden et al.*, 2009] at three sites in the TIO. The CERES data agree well with RAMA measurements with the correlation coefficients exceeding 0.90 at all the three buoy sites. The mean values and standard deviation (STD) from CERES are close to RAMA measurements, but the CERES STD values are smaller by about 15%. Comparisons are also performed for the Pacific Ocean with the Tropical Atmosphere Ocean/Triangle Trans-Ocean Buoy Network (TAO/TRITON) buoys, and we obtained similar degree of consistency.

[14] The 0.25° × 0.25° cross-calibrated multiplatform (CCMP) ocean surface wind vectors available during July 1987–December 2011 [*Atlas et al.*, 2008] are used as wind forcing. Zonal and meridional surface wind stress, τ_x and τ_y, are calculated from the CCMP 10 m wind speed ₁*V*₁ using the standard bulk formula

$$\tau_x = \rho_a c_d |V| u, \tau_y = \rho_a c_d |V| v, \qquad (1)$$

where $\rho_a = 1.175$ kg m⁻³ is the air density, $c_d = 0.0015$ is the drag coefficient, and u and v are the zonal and meridional 10 m wind components. The precipitation forcing is from the 0.25° × 0.25° Tropical Rainfall Measuring Mission (TRMM) Multi-Satellite Precipitation Analysis (TMPA) level 3B42 product [*Kummerow et al.*, 1998] available for 1998–2011. In addition to precipitation, river discharge is also important for simulating upper-ocean salinity distribution in the Bay of Bengal (BoB) [e.g., *Han and McCreary*, 2001], which influences the stratification and circulation of the TIO. In our experiments, we utilize the satellite-derived monthly discharge records of the Ganga-Brahmaputra [*Papa et al.*, 2010] and monthly discharge data from *Dai et al.* [2009] for the other BoB rivers such as the Irrawaddy as the lateral fresh water flux forcing.

2.3. Experiments

[15] The model is spun up for 35 years from a state of rest, using WOA09 annual climatology of temperature and salinity as the initial condition. Data sets described above are averaged into monthly climatology and linearly interpolated onto the model grids to force the spin-up run. Restarting from the already spun-up solution, HYCOM is integrated forward from 1 January 2005 to 30 November 2011. Two parallel experiments are performed, the main run (MR) and the experimental run (EXP), using daily atmospheric forcing fields. The only difference between the
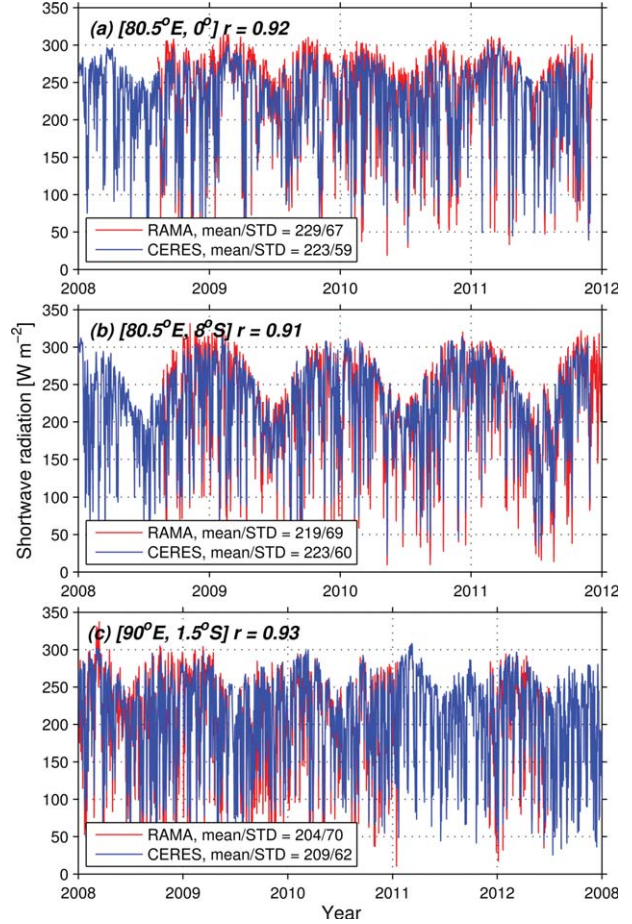

Figure 1. Comparison of daily surface net shortwave radiation Q_{SW} (W m⁻²) between the CERES data set (blue) and in situ measurements of RAMA buoys (red) at (a) 80.5°E, 0°, (b) 80.5°E, 8°S, and (c) 90°E, 1.5°S. A surface albedo of 3% was applied to the RAMA buoy data before plotting.

MR and EXP is that in the MR an idealized hourly diurnal cycle is imposed on Q_{SW}, which is assumed to be sinusoidal and energy conserving [*Shinoda and Hendon*, 1998; *Schiller and Godfrey*, 2003; *Shinoda*, 2005],

$$Q_{SW}(t) = \begin{cases} \pi Q_{SW0} & \sin\left[2\pi(t-6)/24\right] \text{ for } 6 \leq t \leq 18 \\ 0 & \text{for } 0 \leq t \leq 6 \text{ or } 18 \leq t \leq 24 \end{cases}, \qquad (2)$$

where t is the local standard time (LST) in hours, and Q_{SW0} is the daily mean value of Q_{SW}. Hence, the difference between the MR and EXP isolates the impact of the solar radiation diurnal cycle. Both the two experiments are integrated for around 7 years from January 2005 to November 2011, with the outputs stored in daily resolution. In addition, 0.1 day (2.4 h) output from MR is also stored for the period overlapping the CINDY/DYNAMO field campaign (September-November 2011) to better resolve the ocean diurnal variation. In order to avoid the transitioning effect from the spin up, only the 2006–2011 output is used for analysis. Noted that the 0.25° × 0.25° resolution allows the model to resolve eddies resulting from oceanic internal variability. This effect is contained in the difference solution

MR-EXP and will be discussed in section 5.

3. Model/Data Comparison

3.1. Comparisons With In Situ and Satellite Observations

[16] To validate the model performance, we compare the output of HYCOM MR with available in situ and satellite observations. During the 2006–2011 period, the wintertime mean SST from HYCOM MR is quite similar to that from the TRMM Microwave Instrument (TMI) data [*Wentz et al.*, 2000] (Figures 2a and 2b). In the TIO, both the SCTR (55°–70°E, 12°–4°S) and CEIO (65°–95°E, 3°S–3°N) regions are covered by weak winds and characterized by high SST (> 29°C) values during winter, which are well simulated by the model. Major discrepancies occur in the western tropical Pacific, where the simulated warm pool (SST > 28°C region) is larger in size than TMI observations. The modeled sea surface salinity (SSS) pattern also agrees with the in situ observational data set of the Grid Point Value of the Monthly Objective Analysis (MOAA-GPV) data [*Hosoda et al.*, 2008] (Figures 2c and 2d), which includes data records from Argo floats, buoy measurements, and casts of research cruises. Note that SSS in the MOAA-GPV is represented by salinity at 10 dbar, which is the shallowest level of the data set, whereas HYCOM SSS is near the surface (∼0.26 m). While the model and observation reach a good overall agreement, the MR SSS is somewhat higher in the subtropical South Indian Ocean, Arabian Sea, and western BoB. In the regions of our interest, the SCTR and CEIO, however, the modeled SSS values are close to the observations.

[17] The wintertime mean MLD values from the MOAA-GPV and HYCOM MR agree well in the two key regions (Figure 3). They show consistent large-scale spatial patterns over the Indian Ocean. Here, the MLD is defined as the depth at which the potential density difference $\Delta\sigma$ from the surface value is equal to a equivalent temperature decrease of 0.5°C [*de Boyer Montégut et al.*, 2004],

$$\Delta\sigma = \sigma(T_0\text{-}0.5, S_0, P_0) - \sigma(T_0, S_0, P_0), \qquad (3)$$

where T_0, S_0, and P_0 are temperature, salinity, and pressure at the sea surface, respectively. Apparent discrepancies occur in the southeastern TIO, Arabian Sea, and BoB, where the modeled MLD is systematically deeper than the observations by about 10–20 m. Possible causes for this difference are uncertainties in the forcing fields that may result in errors in oceanic stratification and mixing and model parameterization of turbulent mixing.

[18] The seasonal cycle and interannual variations of modeled SST averaged over the Indian Ocean also agree with TMI data (Figure 4a). There is a mean warming bias of ∼0.26°C during the experiment period (2005–2011), which arises mainly from boreal summer (May-October) SST bias. During winter, however, the model and satellite observation agree well (Figure 4a). The vertical temperature profiles averaged in the SCTR and CEIO regions from the MR show general agreements with the MOAA-GPV data set (Figures 4b and 4c), with model/data deviations occurring primarily in the thermocline layer. The model has a more diffusive thermocline and thus shows artificial
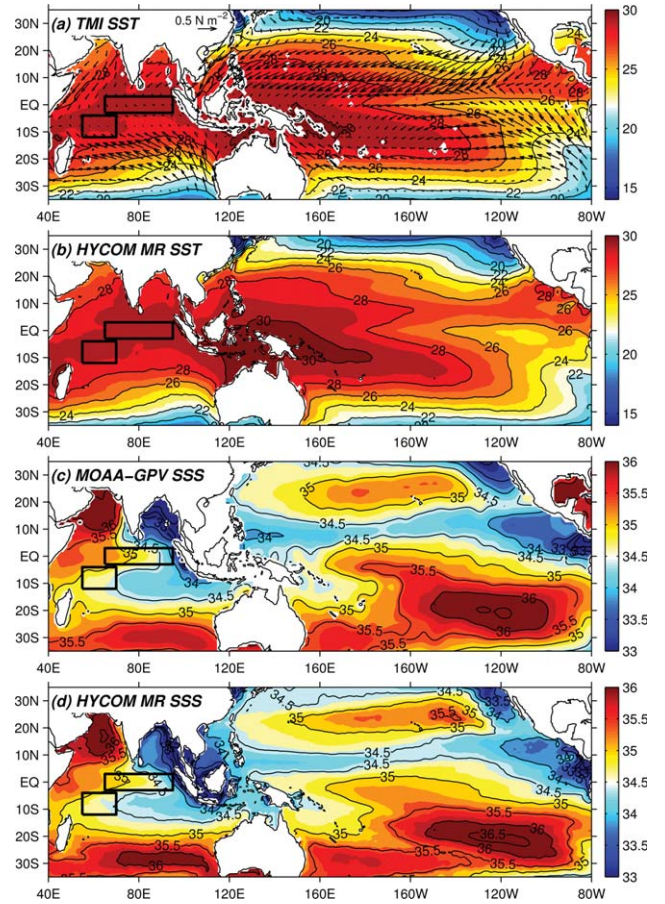

Figure 2. Mean wintertime (November–April) SST (°C) from (a) TMI satellite observation and (b) the HYCOM MR. Black vectors in Figure 2a denotes the mean wintertime CCMP wind stress (N m^{-2}). Mean wintertime SSS (psu) from (c) the MOAA-GPV data set and (d) the HYCOM MR. In all panels, variables are averaged for the period of January 2006–November 2011. The two black rectangles denote the areas of the SCTR (55°–70°E, 12°–4°S) and CEIO (65°–95°E, 3°S–3°N) regions.

warming between 100 and 400 m, which is a common bias among most existing OGCMs.

[19] Daily time series of modeled SST, which includes variability from synoptic to interannual timescales, at two RAMA buoy locations (67°E, 1.5°S within the SCTR and 80.5°E, 1.5°S within the CEIO) are compared with the RAMA and TMI observations in Figure 5. MR/RAMA correlations are 0.72 at the SCTR location and 0.85 at the CEIO location, which are higher than the corresponding MR/TMI correlation values (0.65 and 0.61). It is noticeable that the TMI SST (red curves) exhibits intensive high-frequency warming/cooling events which are absent in both the HYCOM MR and RAMA buoy observation. Correspondingly, in the spectral space, although intraseasonal SST variances at 20–90 day period are statistically significant at 95% level in all the three data sets, the power at 20–50 day period is visibly higher in TMI than in the other two (Figures 5b and 5d). The variances of the HYCOM MR and RAMA buoys agree quite well with each other in both temporal and spectral spaces. Differences among data sets
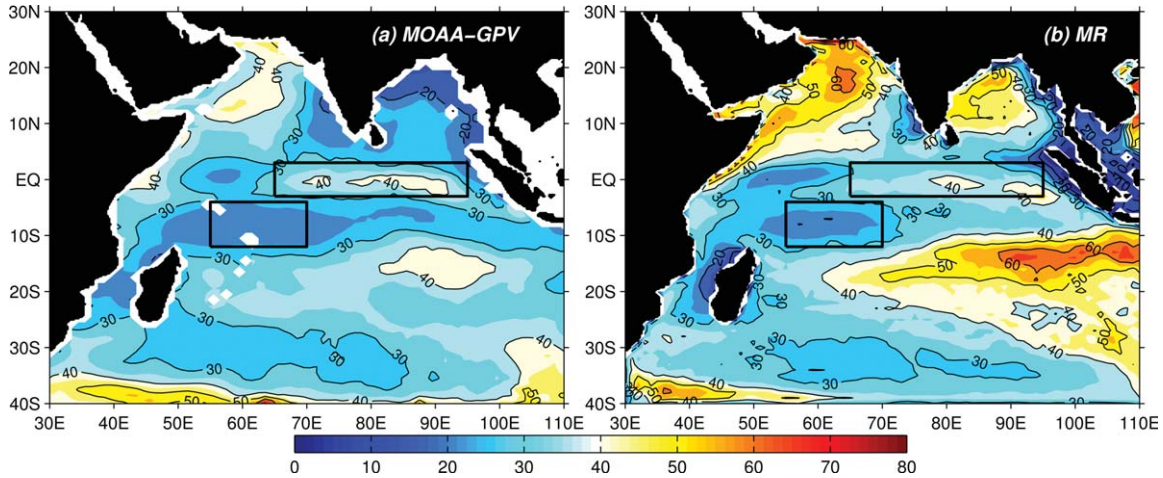
Figure 3. Mean wintertime MLD (m) in the Indian Ocean basin during 2006–2011 from (a) the MOAA-GPV data set and (b) HYCOM MR. Black contours' interval is 10 m. The two black rectangles denote the SCTR and CEIO.

may arise from the definition of SST. The satellite microwave instruments measure the skin temperature of the ocean, which contains the signals of skin effect that can often reach several degrees of variability amplitudes [*Saunders*, 1967; *Yokoyama et al.*, 1995; *Kawai and Wada*, 2007]. The modeled and buoy-measured SSTs represent temperatures at 0.26 m and 1.5 m, respectively, which contain little impact from the skin effect.

3.2. Comparison With CINDY/DYNAMO Field Campaign Data

[20] Oceanic in situ measurements of the CINDY/DYNAMO field campaign cover the period of September 2011–March 2012. Our HYCOM simulation, however, ends on 29 November 2011 due to the availability of forcing fields, particularly CERES radiation and CCMP winds. Consequently, the comparison will focus on their overlap-

ping period of September-November 2011 (referred to as "the campaign period" hereafter). Figure 6 shows the time series during the campaign period at 95°E, 5°S where hourly RAMA buoy temperature record is available. We resample the hourly RAMA 1.5 m temperature records to 0.1 day LST to match our MR output. The amplitudes of simulated SST diurnal cycle and their intraseasonal variability are well represented by the model. Both the model and observations show amplified diurnal cycle amplitudes during 25 September–5 October, 10–16 October, 3–16 November, and 22–26 November, and weakened amplitudes during the remaining periods. It is discernible that large (small) $dSST$ values occur during intraseasonal warming (cooling) periods, which will be further investigated in section 4. Note that there are several large diurnal warming events with $dSST > 1°C$ in the MR 0.26 m temperature (blue curve), which correspond to much weaker amplitudes
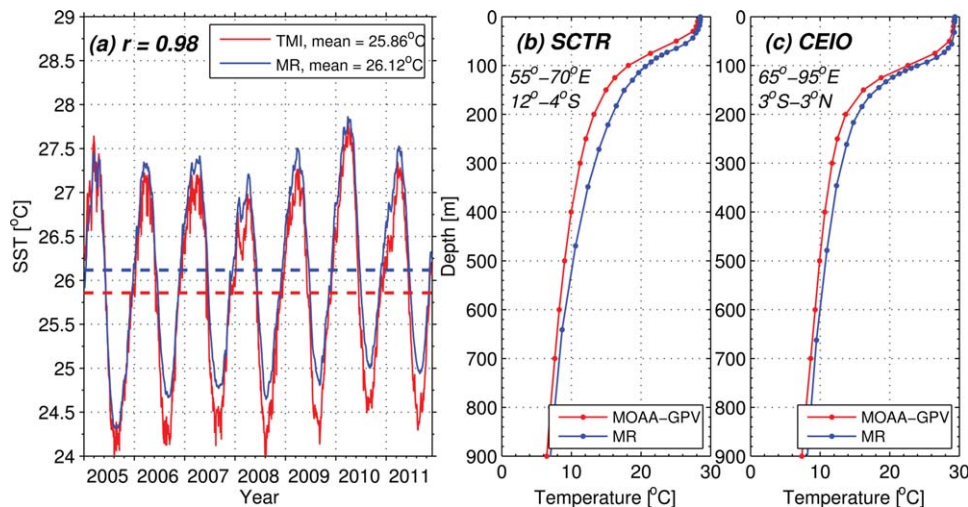

Figure 4. (a) SST time series (°C) averaged over the Indian Ocean basin (30°–110°E, 36°S–30°N) from TMI (red solid) and HYCOM MR (blue solid). The dashed straight lines denote their 2005–2011 mean values. (b) Mean temperature profiles for the SCTR region from the MOAA-GPV data set (blue) and HYCOM MR (red). (c) Same as Figure 4b but for the CEIO region.
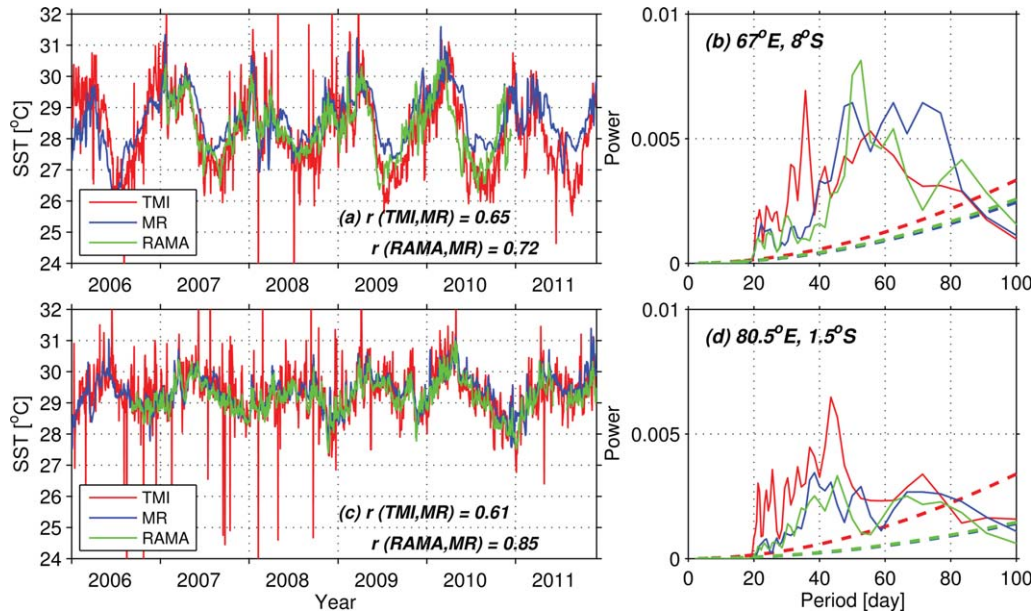
Figure 5. Comparison of SST time series from RAMA buoys' in situ measurements (green), TMI satellite observations (red), and HYCOM MR output (blue) at two sites representing (a) the SCTR region (67°E, 1.5°S) and (c) the CEIO region (80.5°E, 1.5°S. (b) and (d), Their corresponding power spectrums (solid lines), with the dashed lines denoting 95% significance level. Here, power spectrums are calculated after a 20–90 day Lanczos band-pass filter to highlight the intraseasonal signals. SST of RAMA buoys are measured at 1.5 m depth.

in the RAMA 1.5 m temperature (red curve). The MR 1.5 m temperature (green curve) confirms that those large *dSST* signals are due to the formation of the thin diurnal warm layer (compare the blue and green curves) [e.g., *Kawai and Wada*, 2007]. These large events occur in November when maximum solar insolation and the ITCZ migrate to the southern TIO. Enhanced insolation and relaxed winds give rise to large diurnal warming events based on the results from previous observational studies.

[21] The upper-ocean thermal structure and its temporal evolution are reasonably simulated by HYCOM during the DYNAMO field campaign at two buoy locations in the CEIO (Figures 7a–7d). For example, the vertical displacements of the MLD (blue curve) are generally consistent with buoy observations, albeit with detailed discrepancies, which are partly attributable to internal variability of the ocean. The modeled thermocline, however, is more diffusive than the observations, consistent with Figure 4. The intraseasonal variations of SST associated with the MJO events are well reproduced by the model, with a linear correlation exceeding 0.8 at both sites, even though the cooling during 26 October–10 November at 79°E, 0° (Figure 7e) is significantly underestimated.

[22] In this section, we have validated the model with independent observational data sets based on satellite, buoy, and Argo measurements. The comprehensive comparison demonstrates that albeit with some biases, HYCOM is able to properly simulate the TIO upper-ocean mean state and variability at various timescales, and thus can be used to examine the impact of the diurnal cycle of solar radiation on the intraseasonal mixed layer variability associated with MJO events.

4. Effects of Diurnal Cycle on the TIO

4.1. Effects During the 2006–2011 Period

4.1.1. Impacts on the Mean Fields

[23] To isolate the impact of the diurnal cycle of solar radiation, we examine the difference solution MR-EXP. Figure 8a shows the wintertime mean daily SST difference, ΔSST, where the symbol "Δ" denotes the difference between MR and EXP for daily mean variables. Consistent with previous studies based on 1-D model solutions (section 1.2), the diurnal cycle leads to a general surface warming and thus increases the mean SST in the TIO north of 10°S and the western equatorial Pacific. In the SCTR and
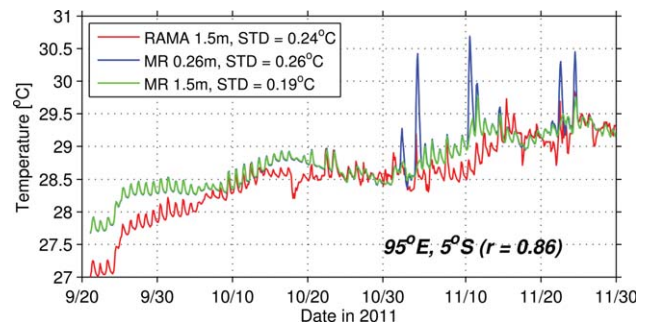

Figure 6. The 1.5 m temperature (°C) measured by a RAMA buoy (red) and HYCOM MR 0.26 m temperature (blue) and 1.5 m temperature (green) at 95°E, 5°S during the CINDY/DYNAMO field campaign period covered by our model simulation. Data are presented in 0.1 day resolution.
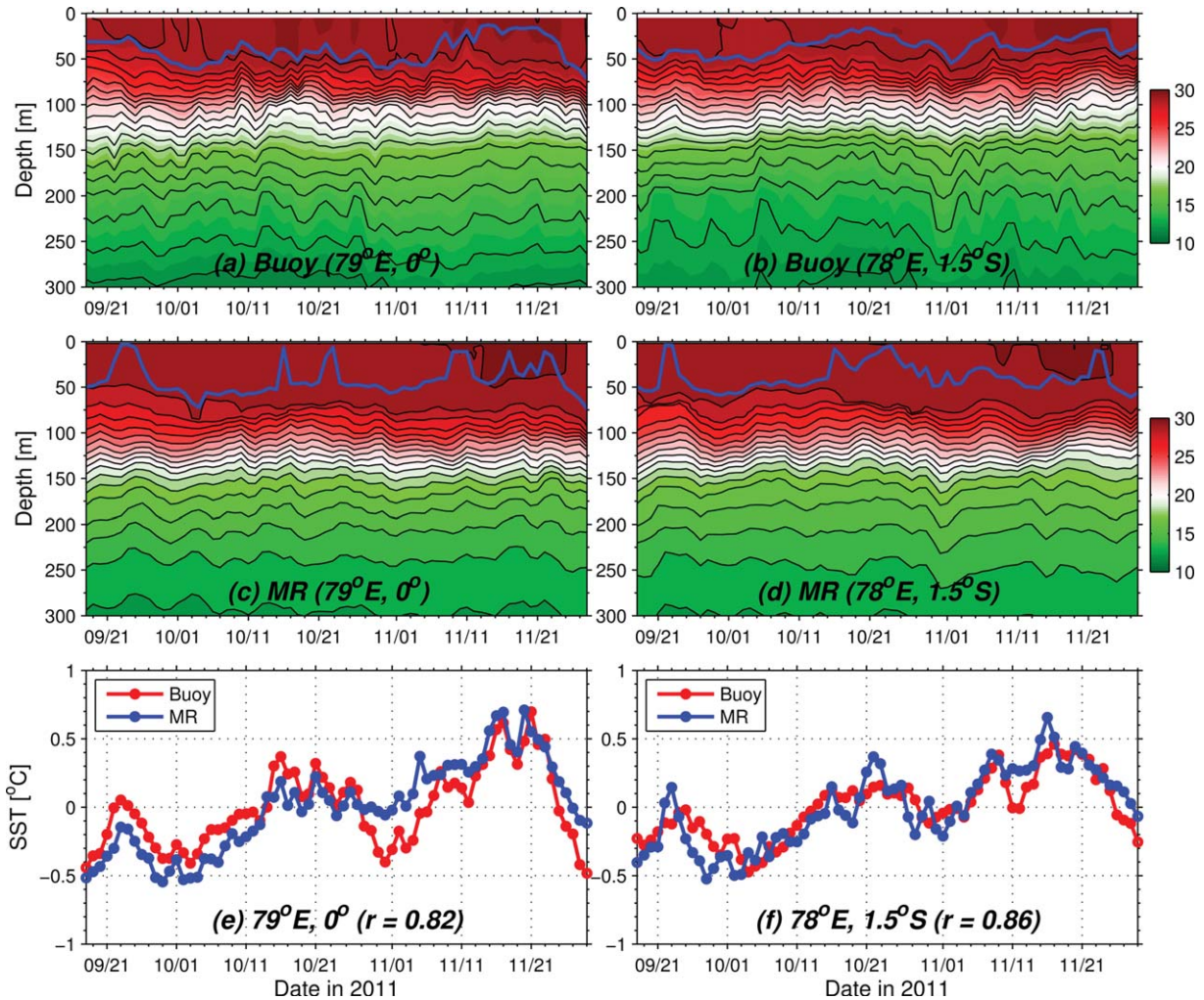
Figure 7. Depth-date maps of daily temperature (°C) from DYNAMO buoys at (a) 79°E, 0° and (b) 78°E, 1.5°S, with the MLD highlighted with blue curves. (c and d) The corresponding maps from HYCOM MR. (e and f) The daily SST anomaly (°C) from DYNAMO buoys (red) and HYCOM MR (blue) at the two buoy sites are compared.

CEIO regions, the warming effect exceeds 0.1°C, and the mean MLD is shoaled by around 4–8 m (Figure 8b). In the BoB and central-eastern Indian Ocean south of 10°S, MLD is deepened. In most areas, deepened (shoaled) MLD corresponds to decreased (increased) SST. This is consistent with the fact that a deepened MLD involves entrainment of colder water and thus leads to SST cooling. An exception is in the central-northern BoB, where the diurnal cycle causes MLD deepening by ∼10 m but SST increasing. This may be attributable to the strong haline stratification near the surface due to monsoon rainfall and river discharge, which leads to the existence of the barrier layer and temperature inversion [e.g., *Vinayachandran et al.*, 2002; *Thadathil et al.*, 2007; *Girishkumar et al.*, 2011]. As a result, relatively warmer water is entrained to the surface mixed layer by the diurnal cycle. To confirm this point, we checked the mean vertical temperature and salinity profiles in the model output. Comparing to those in the Arabian Sea and the subtropical South Indian Ocean, the mean vertical temperature gradient in the upper 100 m is much smaller in the central-northern BoB. The stratification in this region relies greatly

on salinity gradient; and vertical temperature inversions often occur (not shown; also see *Wang et al.* [2012b]). Such vertical temperature distribution favors the rectified warming effect by the diurnal cycle.

4.1.2. Impacts on Intraseasonal SST

[24] To achieve our goal of understanding the diurnal cycle effect on intraseasonal SST variability associated with the MJO, we first apply a 20–90 day Lanczos digital band-pass Filter [*Duchon*, 1979] to isolate intraseasonal SST variability. The wintertime STD maps of 20–90 day SST from TMI satellite observation and HYCOM MR are shown in Figures 9a and 9b. The model, however, generally underestimates the amplitude of intraseasonal SST variability. In the SCTR and CEIO regions, the underestimation is about 20%. This model/data discrepancy is attributable to at least two factors. First, TMI measures the skin temperature of the ocean, which has larger intraseasonal variability amplitudes than the bulk layer temperature (see Figure 5). Second, the somewhat underestimation of radiation variability in CERES data set (Figure 1) and uncertainty in
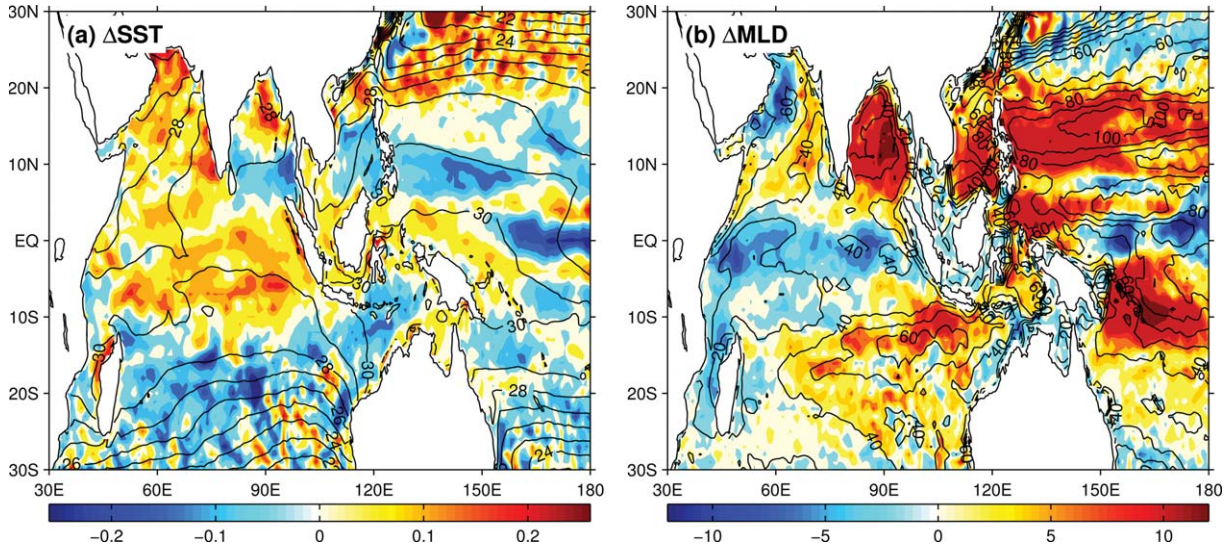
Figure 8. Mean fields of (a) SST difference (color shading; in °C) and (b) MLD difference (color shading; in m) between MR and EXP, i.e., ΔSST and ΔMLD, in winter. Black contours denote mean winter SST and MLD from MR.
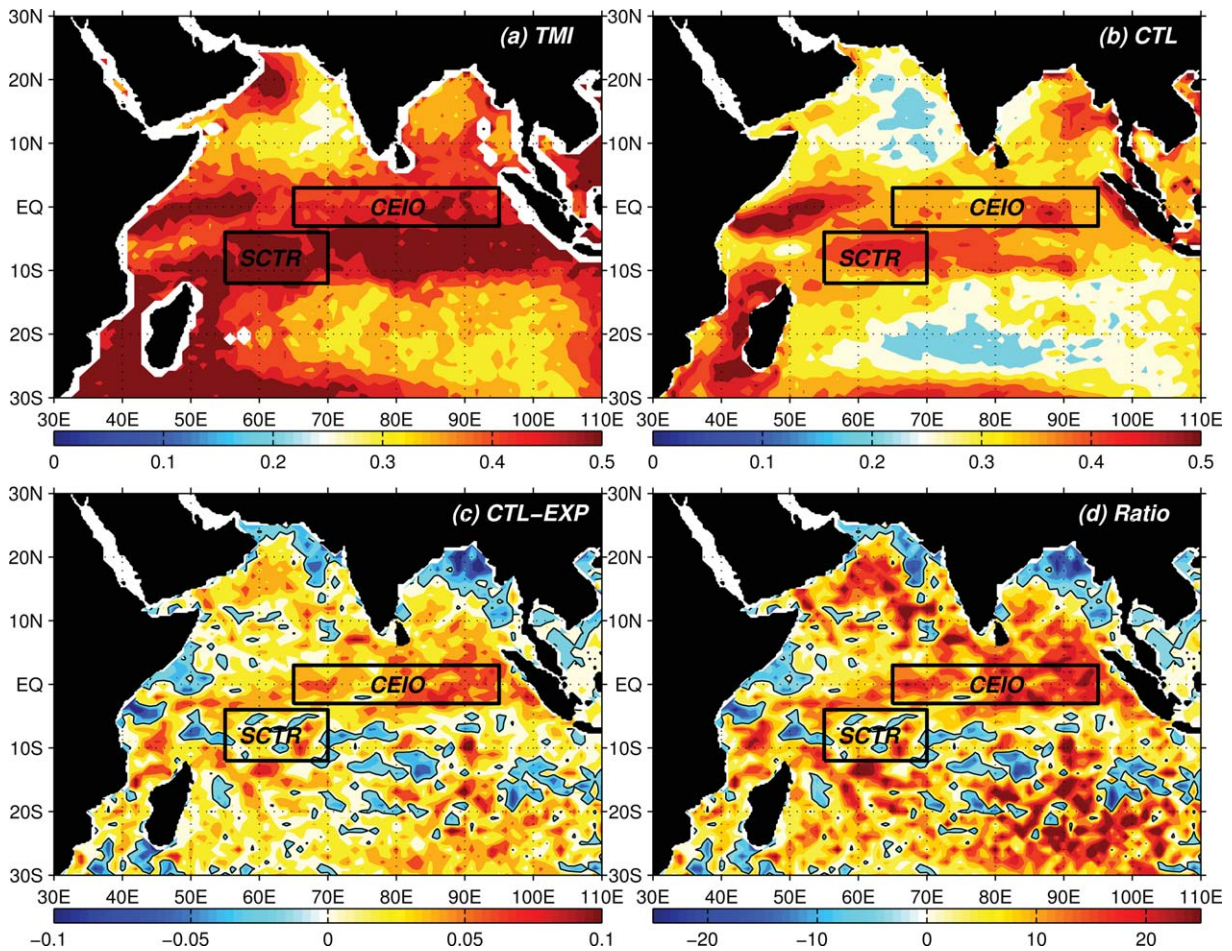

Figure 9. STD maps of 20–90 day SST (°C) from (a) TMI and (b) MR. (c) The difference of 20–90 day SST STD (°C) between MR and EXP and (d) its ratio (%) relative to the EXP value. The two black rectangles denote the areas of the SCTR and CEIO. All the STD values are calculated for winter months (November–April) in 2006–2011.
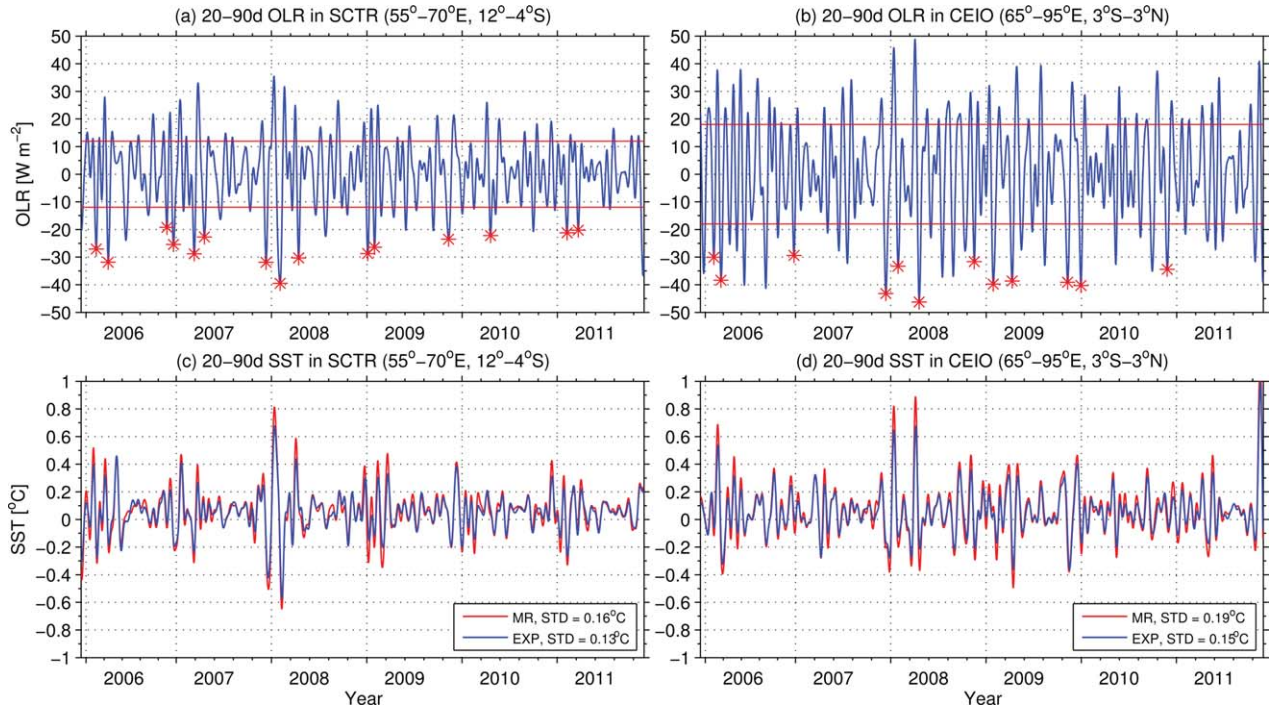
Figure 10. The 20–90 day OLR (W m^{-2}) averaged over (a) the SCTR region and (b) the CEIO region. The red straight lines indicate one STD value range. Wintertime OLR minima with magnitude exceeding 1.5 STD value are highlighted with red asterisks. Time series of 20–90 day SST (°C) from MR (red) and EXP (blue) averaged over (c) the SCTR region and (d) the CEIO region.

other forcing fields may also contribute. In spite of the quantitative differences, the general patterns of STD from HYCOM MR agree with satellite observation.

[25] The diurnal cycle acts to enhance 20–90 day SST variability in most regions of the TIO, as shown by the STD difference between the MR and EXP (Figure 9c). In the SCTR and CEIO regions, the strengthening magnitude exceeds 0.05°C at some grid points. To better quantify such impact, we calculate the ratio of STD difference relative to the STD value in EXP (Figure 9d),

$$\text{Ratio} = \frac{STD_{MR} - STD_{EXP}}{STD_{EXP}} \times 100\%, \qquad (4)$$

where STD_{MR} and STD_{EXP} are the 20–90 day SST STDs from MR and EXP, respectively. The ratio generally exceeds 15% and occasionally reaches 20%–30% in some areas of the CEIO. In the SCTR, the overall ratio is positive but pattern is incoherent, with positive values separated by negative ones. Similar incoherent patterns are seen in other regions, such as near the Somalia coast and in the central-eastern South Indian Ocean. Such incoherence is likely induced by oceanic internal variability [e.g., *Jochum and Murtugudde*, 2005; *Zhou et al.*, 2008], which show differences between MR and EXP due to their nonlinear nature. As a result, the effect of internal variability is contained in the MR-EXP solution.

[26] To reduce the internal variability effect and focus on the pure oceanic response to the MJO forcing, we examine the area-averaged properties over the SCTR and CEIO regions. To identify the strong intraseasonal convection events associated with the MJO and the corresponding SST

variability, we obtain the time series of 20–90 day satellite-derived outgoing longwave radiation (OLR) from the National Oceanic and Atmospheric Administration (NOAA) [*Liebmann and Smith*, 1996] averaged over the SCTR and CEIO regions, along with the area-averaged 20–90 day SST from MR and EXP (Figure 10). The 20–90 day OLR and SST have a close association, with all large SST variability events corresponding to strong OLR fluctuations. The lead-lag correlation between OLR and SST during winters of 2006–2011 is significant, with peak values of $r > 0.60$ in both regions when OLR leads SST by 3–4 days. These results suggest that the large-amplitude wintertime intraseasonal SST variability results mainly from the MJO forcing. Both the 20–90 day OLR and SST show clear seasonality in the SCTR, with most strong events happening in winter [*Waliser et al.*, 2003; *Han et al.*, 2007; *Vialard et al.*, 2008]. Similar seasonality is discernible in the CEIO, although less prominent. The wintertime correlation of 20–90 day OLR time series between the two regions is $r = 0.48$ (significant at 95% confidence level) when the SCTR OLR leads the CEIO one by 2–3 days. This indicates that some of the wintertime MJO events initiated in the SCTR region have a large down-stream signature in the CEIO. The diurnal cycle effect on SST is significant in both regions (Figure 10), increasing the STD values by 0.03°C and 0.04°C respectively, which means an enhancement of intraseasonal SST variability by $> 20\%$ relative to EXP values. This magnitude is close to the estimations of 20%–30% in the western Pacific warm pool [*Shinoda and Hendon*, 1998; *Bernie et al.*, 2005, 2007] and tropical Atlantic Ocean [*Guemas et al.*, 2011].

[27] Diurnal ocean variation is believed to be potentially important for the air-sea interaction of the MJO, primarily
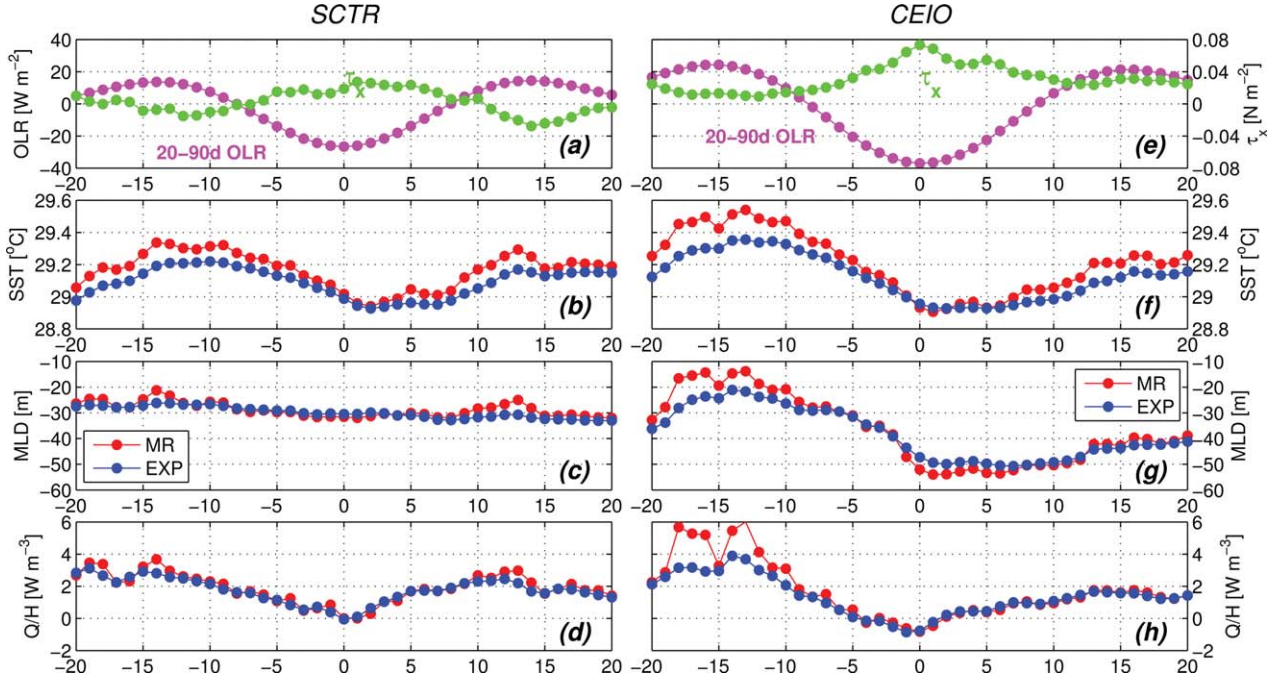
Figure 11. Evolutions of (a) 20–90 day OLR (pink; in W m^{-2}) and unfiltered τ_x (green; in N m^{-2}), (b) SST (in °C), (c) MLD H (m), and (d) mean mixed layer heating Q/H (W m^{-3}) of the composite wintertime MJO event in the SCTR region. In Figures 11b–11d, red (blue) curves denote variables of MR (EXP). (e–h) Same as Figures 11a–11d but for the CEIO region.

because its rectification on daily mean SST helps to trigger atmospheric convection. To estimate the diurnal cycle impact during different phases of the MJO, we perform a composite analysis based on the 20–90 day OLR values. There are 15 wintertime convection events with 20–90 day OLR reaching minimum (negative) and exceeding 1.5 STD during 2006–2011 in SCTR and 12 events in CEIO region (Figures 10a and 10b), which are used to construct the composite fields. The days with OLR minima are taken as the 0 day phase. Then a 41 day composite MJO event is constructed by simply averaging variables for each day between −20 day and +20 day. Variations of the SCTR region during the composite MJO are shown in Figure 11. The 20–90 day OLR shows two maxima at around the −14 and 14 day, remarking the calm stages of the composite MJO. The total zonal wind (unfiltered) is very weak in the SCTR region (also see Figure 2a) and changes sign with the MJO phases, showing easterlies at the calm stage ($\tau_x = -0.02$ N m^{-2}) and westerlies at the wet stage (the 0 day) ($\tau_x = 0.02$ N m^{-2}). There is no large difference in wind speed between the calm and wet phases, and therefore the *dSST* magnitude is primarily controlled by insolation. The diurnal cycle induces > 0.1°C SST increase and ∼5 m MLD decrease during the calm stage. During the wet phase, *dSST* is smaller due to the reduced insolation by MJO-associated convective cloud, which results in little rectification on daily mean SST (Figure 11b). The slight deepening of MLD induced by the diurnal cycle (Figure 11c) leads to an entrainment cooling, which also acts to compensate the rectified SST warming by the diurnal cycle.

[28] The situation is generally similar in the CEIO except for more prominent changes in wind speed (Figure 11e).

The preconditioning calm stage is dominated by weak westerlies with $\tau_x = 0.01$ N m^{-2} at −15 day. At the wet phase, the westerly wind stress reaches 0.06–0.08 N m^{-2}. Together with changes in insolation, the calm/wet difference in *dSST* is larger in the CEIO. Consequently, the rectification of the diurnal cycle onto intraseasonal SST variation is larger. During the calm phase, ΔSST reaches as large as 0.2°C, whereas at the wet phase ΔSST is very small (Figure 11f). Also different from the SCTR region, the calm stage after the passage of convection center, e.g., during the 12–20 day, is characterized by westerly winds with $\tau_x = 0.03$–0.04 N m^{-2}. The relatively strong winds suppress diurnal ocean variation and its rectification onto the daily mean SST and MLD. In both regions, the changes of ΔSST can be well explained by MR-EXP difference in the mean mixed layer heating, e.g., the total heat flux Q divided by MLD H (Figures 11d and 11h). This result suggests that in the TIO the diurnal cycle effect on intraseasonal SST variability is primarily through one-dimensional nonlinear rectification via thinning the mixed layer at the calm phase. The entrainment induced by the diurnal cycle also seems contribute to intraseasonal SST variability by cooling daily mean SST at the wet stage, but its role is secondary.

4.2. Effects During CINDY/DYNAMO Field Campaign

[29] The mean patterns of *dSST*, which is defined as the difference between the MR SST maximum between 10:30 and 21:00 LST and the preceding minimum between 0:00 and 10:30 LST in each day, along with shortwave radiation Q_{SW} and zonal wind stress τ_x, during the campaign period (16 September–29 November 2011) are shown in Figure

12. The diurnal warming is large ($dSST = 0.6$–$0.9°C$) along the equator and small ($dSST = 0.1$–$0.3°C$) over large areas of the South Indian Ocean (Figure 12a). There is a visible resemblance between $dSST$ pattern with mean Q_{SW} (Figure 12b, which also indicates the diurnal cycle amplitude of Q_{SW}) and wind speed (Figure 12c). For example, large $dSST$ values ($> 0.9°C$) in the western equatorial basin, the Mozambique Channel, the Sumatra coast, and marginal seas between Indonesia and Australia all correspond to high Q_{SW} and low wind speed. Both the CEIO and SCTR regions are covered with small Q_{SW} values (< 240 W m^{-2}), but the CEIO is dominated by weak westerly winds, while the SCTR is with strong easterly winds, which leads to a much larger $dSST$ in the CEIO compared to the SCTR region.

[30] During the campaign period, eastward propagation of the 20–90 day OLR signals is quite clear near the equator (Figure 13e) but is less organized within the SCTR latitudes (Figure 13a). Therefore, we define the stages of the MJO events with respective to OLR value in the CEIO region. Two MJO events occurred during the campaign period: MJO 1 and MJO 2. The calm stage of MJO 1 (CM-1) is characterized by positive OLR during 1–11 October (Figure 13e). It develops during 11–21 October (DV-1), reaches the wet phase (WT-1) during 21–29 October, and decays during 29 October–8 November (DC-1). Our model simulation covers only half of MJO 2: 8–15 November is its calm stage (CM-2); and 15–29 November is its developing stage (DV-2). Note that during DV-2, a well-organized strong convection center with 20–90 day OLR < -30 W m^{-2} has formed in the SCTR region (Figure 13a), which propagates eastward and reaches the CEIO near the end of our simulation period. While the wind changes associated with MJO 1 are rather disordered, convection center of MJO 2 is accompanied by organized westerly anomaly (relative to the mean easterly wind) over the SCTR (Figure 13b). Daily maps of 20–90 day OLR (figures not shown) reveal that convection of MJO 1 is centered north of the equator and shifts northward while propagating eastward, suggesting that MJO 1 in October features a typical summertime MJO [e.g., *Waliser et al.*, 2004; *Duncan and Han*, 2009; *Vialard et al.*, 2011]. In contrast, MJO 2 is initiated in the SCTR region in November and developed mainly south of the equator, showing typical features of wintertime MJOs.

[31] In the map of SSTA for the SCTR, the most evident signal is the seasonal warming from boreal summer to winter (Figure 13c). The only well-organized intraseasonal signature in the SCTR region is the warming during 11–21 November following CM-2 and the subsequent cooling induced by MJO 2. Despite an overall basinwide warming rectification by the diurnal cycle, ΔSST is in fact negative for the SCTR area during most days in September and October (Figure 13d). There are striking westward propagating signals in ΔSST, which exert visible influence on SSTA (Figure 13c). These signals are likely manifestation of ocean internal variability. In the CEIO, the mean winds are weak westerlies during the campaign period (also see Figure 12c). Hence, the eastward propagating westerly wind anomalies following the convection centers (Figure 13f) increase the wind speed. The SSTA pattern is clearly dominated by eastward propagating intraseasonal signals associated with the MJOs (Figure 13g), with a visible phase lag
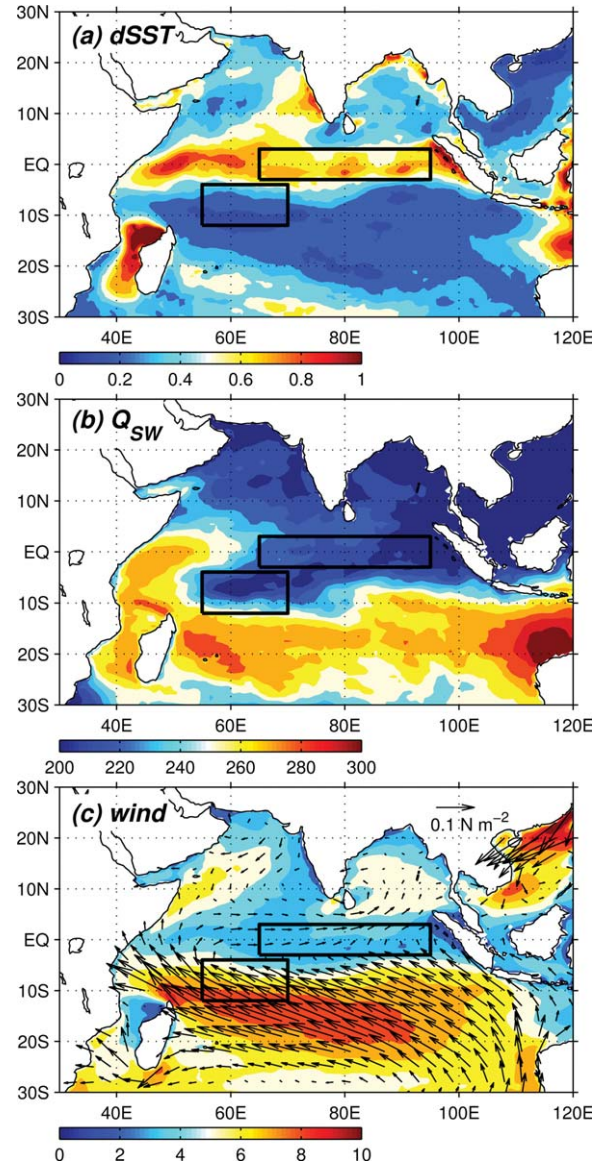

Figure 12. Mean fields of (a) surface diurnal warming $dSST$ (°C), (b) shortwave radiation Q_{SW} (W m^{-2}), and (c) wind speed (color shading; in m s^{-1}) and wind stress (black vectors; in N m^{-2}) during the campaign period (16 September–29 November 2011). Here $dSST$ is defined as the difference between the MR SST maximum between 10:30 and 21:00 LST and the preceding minimum between 0:00 and 10:30 LST in each day. The two black rectangles denote the SCTR and CEIO.

of several days to the 20–90 day OLR. Comparing with that in the SCTR region, ΔSST in the CEIO has more systematical contribution to intraseasonal SSTA and amplifies its variability amplitude. For example, large positive ΔSSTs are seen during CM-1, DV-1, CM-2, and DV-2, while near-zero values occurring at WT-1 and DC-1.

[32] To reduce the influence of ocean internal variability, we average all the relevant properties over the two regions (Figure 14). In agreement with the preceding analysis, the SCTR region exhibits apparent seasonal transitioning. The easterly winds relax with time (Figure 14a), and SST
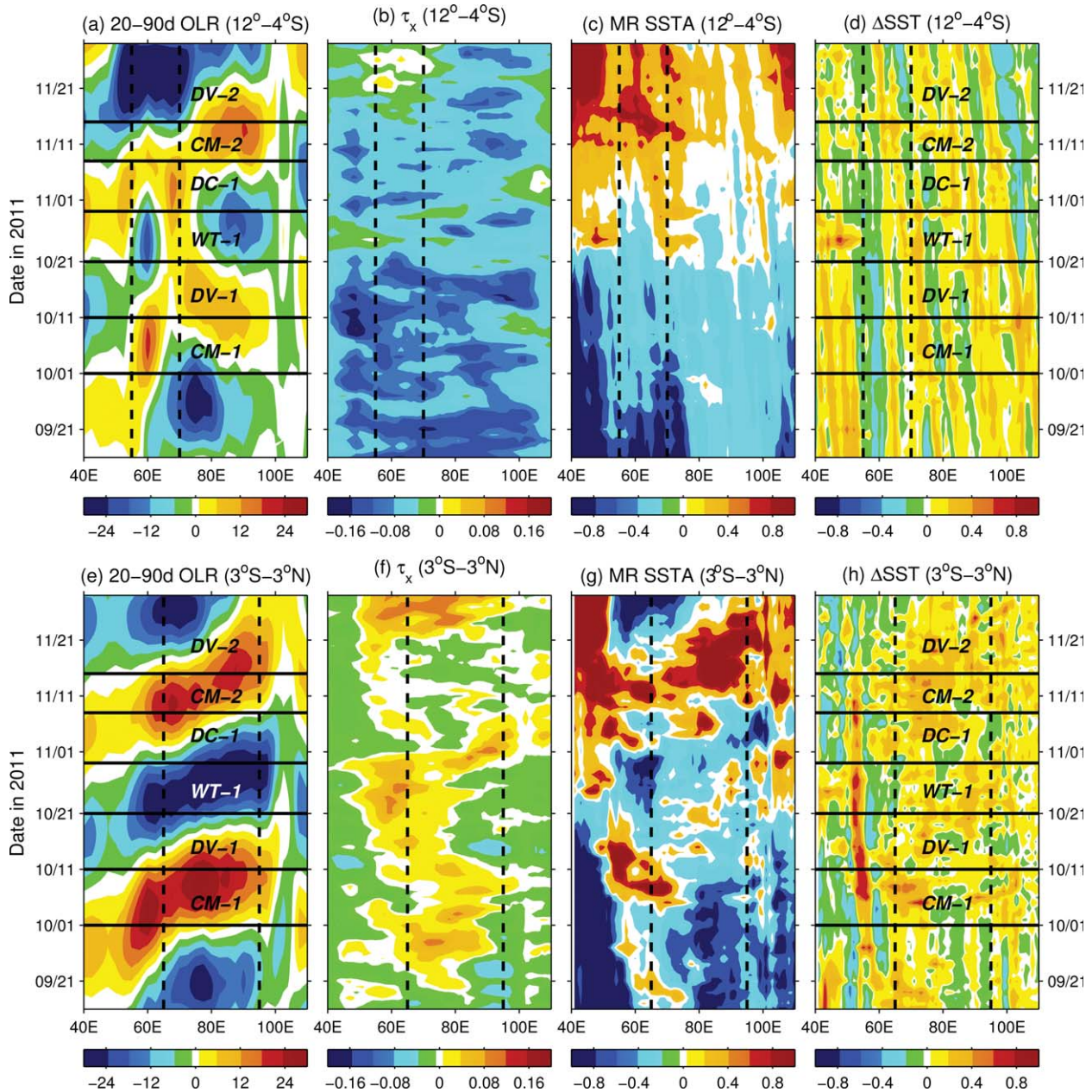
Figure 13. (top) Time-longitude plots of (a) 20–90 day OLR (W m^{-2}), (b) unfiltered zonal wind stress τ_x (N m^{-2}), (c) MR SSTA (°C), and (d) ΔSST (in °C) averaged in the latitude range of the SCTR (12°–4°S). The two dashed lines indicate the longitude range of the SCTR (55°–70°E). (bottom) Same as the top figure but in the latitude range of the CEIO (3°S–3°N), with the two dashed lines indicating its longitude range (65°–95°E). We defined six stages based on the 20–90 day OLR value in the CEIO region: 1–11 October, the calm stage of MJO 1 (CM-1); 11–21 October, the developing stage of the MJO 1 (DV-1); 21–29 October, the wet stage of the MJO 1 (WT-1); 29 October–8 November, the decaying stage of MJO 1 (DC-1); 8–15 November, the calm stage of MJO 2 (CM-2); and 15–29 November, the developing stage of MJO 2.

increases by about 1.3°C during the campaign period (Figure 14b). From September to October, the diurnal cycle has a slight cooling impact on daily mean SST. The only period with a positive ΔSST is 8–16 November that follows the calm stage of MJO 2. After that ΔSST is weak and negative again when the convection center forms. The diurnal cycle amplifies the intraseasonal SST variability for MJO 2 in the

SCTR, but the process is somewhat different from the composite MJO, which has near-zero ΔSST at the wet phase. Figures 14c and 14d suggest that while Q/H is not associated with the cooling, the deepened MLD may be responsible. Under strong easterly winds during this period, $dSST$ is small, and MLD is deeper than that in the composite winter MJO event (Figure 11c). Entrainment induced by the
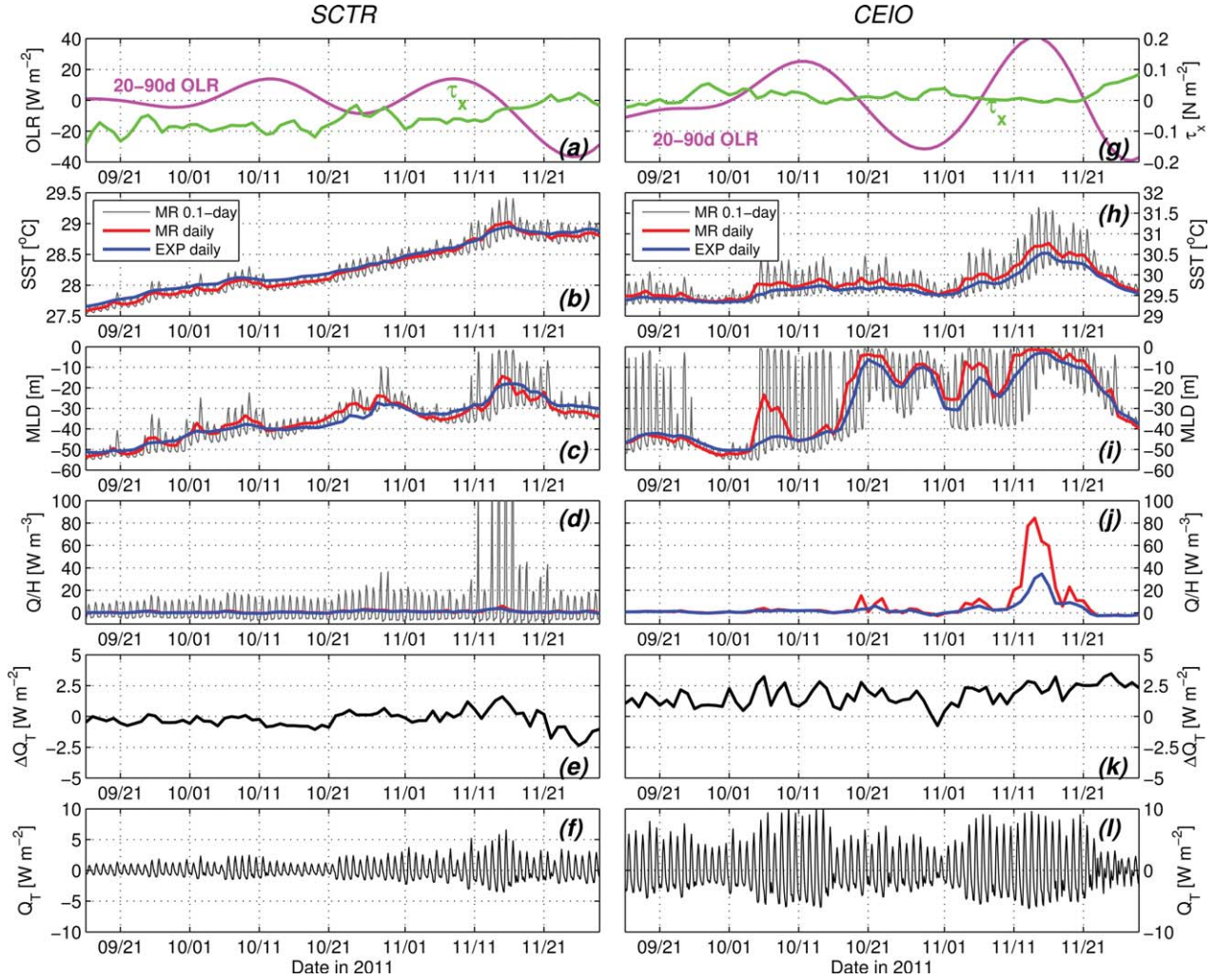
Figure 14. Evolutions of (a) 20–90 day OLR (pink; in W m^{-2}) and unfiltered τ_x (green; in N m^{-2}), (b) SST ($^{\circ}$C), (c) MLD H (m), (d) mean mixed layer heating Q/H (W m^{-3}), (e) the MR-EXP difference in daily upward turbulent heat flux ΔQ_T (W m^{-2}), and (f) the Q_T diurnal cycle (W m^{-2}) averaged in the SCTR region. In Figures 14b–14d, gray, red, and blue curves respectively denote the variables from 0.1 day MR output, daily MR output, and daily EXP output. (g–l) Same as Figures 14a–14f but for the CEIO region.

diurnal cycle brought deeper, colder water into the mixed layer, which acts to overcompensate the weak rectified warming by *dSST*.

[33] In the CEIO, the mean winds are weak, with westerly anomalies following the OLR minima (Figure 14g). The CEIO satisfies low-wind, high-insolation condition at the calm stages and high-wind, low-insolation condition at the wet stages. *Shinoda et al.* [2013a] indicated that extremely weak winds in the CEIO region are mostly responsible for the large diurnal SST variations. Indeed, *dSST* magnitude at the calm stages is 1 order larger than at the wet stages (Figure 14h), which enlarges intraseasonal SST amplitude by about 20%–30% through nonlinear effect. Even though the diurnal cycle also deepens MLD in the CEIO at the wet stages, the entrainment does not lead to a SST cooling. Checking the vertical temperature structure indicates that the main thermocline is deeper in the CEIO than in the SCTR (figures not shown). Nighttime deepening of MLD does not reach the cold thermocline

water, and thus cannot compensate the rectified warming on daily mean SST by the diurnal cycle.

[34] We further assess the diurnal cycle effects on the surface turbulent heat flux toward the atmosphere Q_T that consists of the latent and sensible heat fluxes, $Q_T = Q_L + Q_S$. The latent and sensible heat fluxes can be roughly estimated with the modeled SST and daily wind speed ıVı using a standard bulk formula,

$$Q_L = \rho_a L_E |V| C_L (q_s - q_a), Q_S = \rho_a C_p |V| C_S (SST - T_a) \quad (5)$$

where $\rho_a = 1.175$ kg m^{-3} is the air density, C_L and C_S are, respectively, latent and sensible heat transfer coefficients and both assigned a value of 1.3×10^{-3}, $L_E = 2.44 \times 10^6$ J kg^{-1} is the latent heat of evaporation, $C_p = 1.03 \times 10^3$ J kg^{-1} K^{-1} is the specific heat capacity of air, q_s is the saturation specific humidity at the sea surface, $q_s = q^*$(SST), where the asterisk symbol denotes saturation, and q_a is the specific humidity of the air and a function of the air

temperature T_a, $q_a = RH\,[q^*(T_a)]$. The relative humidity RH is set to be a value of 80% [*Waliser and Graham*, 1993]. Because T_a closely follows the evolution of SST, we cannot use the daily 2 m T_a of the ERA-Interim to calculate Q_L and Q_S. Instead, an empirical estimation method [*Waliser and Graham*, 1993] is used:

$$T_a = \begin{cases} SST - 1.5^oC & \text{for } SST < 29^oC \\ 27.5^oC & \text{for } SST \geq 29^oC \end{cases}. \qquad (6)$$

[35] The 2.4 h modeled SST from MR are used to calculate the 2.4 h Q_T and then averaged into daily Q_T to get comparison with the daily Q_T from EXP (Figures 14e and 14k). Because wind speed is the same for MR and EXP, the MR-EXP difference in daily Q_T (ΔQ_T) is solely induced by SST difference. In the SCTR, the 11–21 November warming by the diurnal cycle induces an extra heat of 1–2 W m^{-2}, which occurs at the precondition stage of MJO 2. In the CEIO, on the other hand, the diurnal cycle provides a persistent heating of 1–3 W m^{-2} for the atmosphere.

[36] Comparing with the relatively small correction on daily mean Q_T, the strong Q_T diurnal cycle, which is obtained by subtracting the daily mean value, is more striking (Figures 14f and 14l). Due to the large *dSST*, the region-averaged Q_T diurnal difference can reach $O(10$ W m^{-2}) at the precondition stages of the MJO. We have also checked the value at specific grid point. At some grids, the Q_T diurnal difference can occasionally reaches as large as 50 W m^{-2}, which is close to the estimation of *Fairall et al.* [1996]. Given that the total surface heat flux change associated with the MJO is less than 100 W m^{-2} [e.g., *Shinoda and Hendon*, 1998; *Shinoda et al.*, 1998], diurnal Q_T changes with $O(10$ m^{-2}) amplitudes are not negligible for the MJO dynamics. Diurnal heating perturbations with such power can destabilize the low-level atmosphere and contribute to the formation of the MJO convection cluster. For a deeper understanding of how the diurnal variation influences the MJO initiation, air-sea coupling processes at diurnal timescale should be taken into consideration.

5. Discussion and Conclusions

[37] Air-sea interactions in the TIO are believed to be essential in the initiation of MJOs [e.g., *Wang and Xie*, 1998; *Waliser et al.*, 1999; *Woolnough et al.*, 2001; *Zhang et al.*, 2006; *Lloyd and Vecchi*, 2010], but the upper-ocean processes associated with intraseasonal SST variability in response to MJOs are not sufficiently understood. One of them is diurnal ocean variation, which is observed to be prominent in the TIO by satellite SST measurements, and suggested to be potentially important in amplifying intraseasonal SST fluctuations and triggering atmospheric convection perturbations at the preconditioning stage of MJOs [e.g., *Webster et al.*, 1996; *Shinoda and Hendon*, 1998; *Woolnough et al.*, 2000, 2001; *Bernie et al.*, 2005, 2007, 2008; *Bellenger et al.*, 2010]. In this study, this process is examined with two HYCOM experiments forced with mainly daily satellite-based atmospheric data sets for the period 2005–2011. The diurnal cycle is included by imposing an hourly idealized Q_{SW} diurnal cycle in MR, and the diurnal cycle effect is quantified by the difference solution, MR-EXP. The experiments also partly cover the timespan

of CINDY/DYNAMO field campaign. The role of the diurnal cycle in two of the monitored MJO events is particularly evaluated to offer possible contribution for the scientific aim of the DYNAMO program. The model reliability is first validated with available in situ/satellite observations including buoy measurements of the CINDY/DYNAMO field campaign. The HYCOM MR output agrees reasonably well with observations in both mean-state structure and variability at various timescales. Especially, intraseasonal upper-ocean variations associated with MJOs and the SST diurnal cycle in the TIO are reproduced well.

5.1. Discussion

[38] The sensitivity of the model representation of the SST diurnal cycle to solar radiation absorption profile was discussed by *Shinoda* [2005]. He showed that *dSST* magnitude is sensitive to the choice of different water types, which in turn influence the amplitude of intraseasonal SSTA. In this study, we adopt the water type I which represents the clearest water with largest penetrating depth for shortwave radiation [*Jerlov*, 1976] for both experiments. Other water types, such as IA and IB (representing less clear water with smaller penetrating depth), are also used to in other testing experiments to evaluate the sensitivity of our results. Indeed, altering the water type to IA or IB leads to some changes in the diurnal cycle's effect. For example, consistent with the result of *Shinoda* [2005], *dSST* magnitude and its rectification on intraseasonal SSTA are both significantly reduced. Moreover, the mean wintertime ΔSST is changed in magnitude and spatial pattern, with more areas showing negative values. The simulation using water type I achieves the largest degree of consistency with the observation and results of previous studies and is thus adopted in our research. Such sensitivity, however, indicates that to improve the model simulation of the SST diurnal cycle, realistic spatially varying solar radiation absorption based on chlorophyll data should be applied instead of using a constant Jerlov water type over the entire model domain.

[39] Our interpretation of the diurnal cycle effect suffers from the noising influence of ocean internal variability throughout the analysis, which urges us to provide a particular evaluation of such impact in this section. Figure 15 is the map of root-mean-square (rms) SST difference between MR and EXP, which quantifies the MR/EXP SST difference at each grid point. The pattern is distinctly different from Figures 8a and 9c. The high value distribution in Figure 15a reminds us the patches of negative values in Figure 9c. The distribution of high-frequency sea surface height (SSH) variability (Figure 15b) confirms that these regions are characterized by intensive ocean internal variability. It means that at a specific grid point the MR/EXP SST difference may mainly reflect the divergence of internal variability signals between MR and EXP rather than the effect of the diurnal cycle. We therefore choose a small region with pronounced internal variability and weak MJO responses to check: 80°–90°E, 20°–10°S. At the center grid (85°E, 15°S) of this box, MR and EXP show large but weakly correlated 20–90 day SSTs ($r = 0.19$) (Figure 15c), which suggests that they are mainly induced by ocean internal variability rather than atmospheric forcing. However,
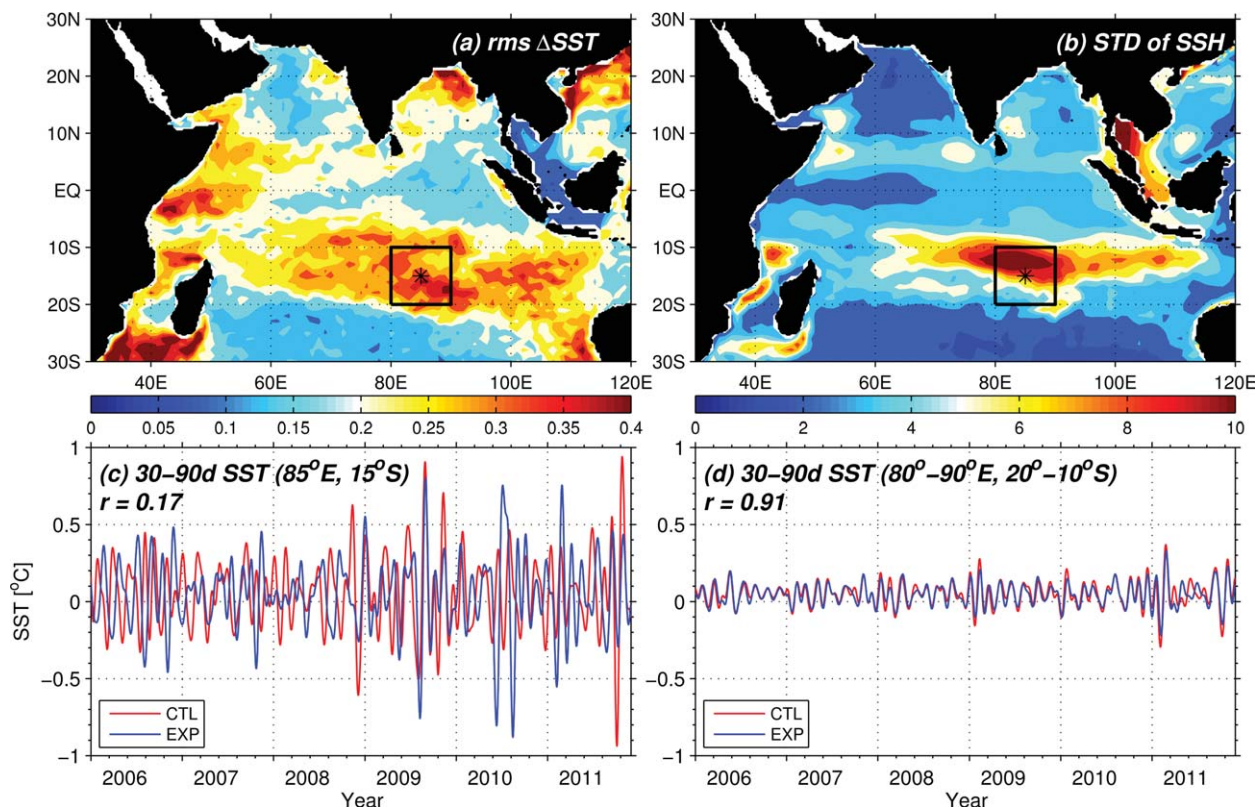
Figure 15. (a) Root-mean-squared (rms) SST difference (°C) between MR and EXP, ΔSST, and (b) STD of 120 day high-passed SSH (cm) from MR in winter. (c) Time series of 20–90 day SST at the site 85°E, 15°S from MR (red) and EXP (blue). (d) Same as Figure 15c but for the 20–90 day SST averaged over the region 80°–90°E, 20°–10°S. The black asterisk and rectangle in Figures 15a and 15b denote, respectively, the site for Figure 15c and region for Figure 15d.

averaged over the box, they are greatly reduced in amplitude but highly correlated with each other ($r = 0.92$) (Figure 15d). These signals are mainly the ocean's responses to atmospheric intraseasonal oscillations like the MJO, and the rectification by the diurnal cycle is clearly manifested. In Figure 13d, we have shown that the diurnal cycle effect on SST in the SCTR is greatly noised by westward propagating signals. Here we further plot out SSH anomalies (SSHA) from MR and EXP at the latitudes of the SCTR (Figure 16). They show generally agreed spatial-temporal patterns, but in fact their difference ΔSSHA is of considerable magnitudes (Figure 16c). The westward propagation speed of ΔSSHA is consistent with that in Figure 13d, confirming the large impact of ocean internal variability on intraseasonal SSTA. However, we have also demonstrated that regional average can effectively reduce such impact and highlight pure ocean responses to atmospheric forcing, especially in a large region like the SCTR where SST responses to MJO events are strong. Therefore, our results derived from analysis of properties averaged for the SCTR and CEIO are generally not largely influenced by ocean internal variability.

[40] Another interesting issue is that during the campaign period, the diurnal cycle effect on intraseasonal SSTA is somewhat different from that in the composite MJO. We attribute this to the background conditions like mean-state winds and MLD. This also indicates the sensitivity of ocean diurnal variation and its rectification to the

ocean/atmosphere background conditions. Our present modeling work covers only 3 months of the CINDY/DYNAMO field campaign and only half of a wintertime MJO event (MJO 2). Analysis of satellite observations suggested that there are three strong winter MJO events occurred during November 2011–March 2012 [*Shinoda et al.*, 2013b; *Yoneyama et al.*, 2013]. With the temporal evolution of background conditions in the TIO, the role of the diurnal cycle in each of these events may be different. Extended model experiments covering the whole campaign period are required to examine this event-by-event variance to accomplish our interpretation. Also worth discussing is the method by which we include diurnal variation into the model. We consider an idealized Q_{SW} diurnal cycle and ignore the diurnal variation of wind and precipitation. A better model presentation of the SST diurnal cycle can be achieved in the future research by considering these factors and compared with empirical parametric model predictions to improve our understanding of the controlling processes [e.g., *Webster et al.*, 1996; *Kawai and Kawamura*, 2002; *Clayson and Weitlich*, 2005]. Realistic simulating and in-depth understanding of the ocean diurnal variation and its feedbacks to the atmosphere will eventually contribute to the improvement of climate model prediction.

5.2. Conclusions

[41] Comparison between MR and EXP outputs reveals that over most areas of the TIO, the diurnal cycle of
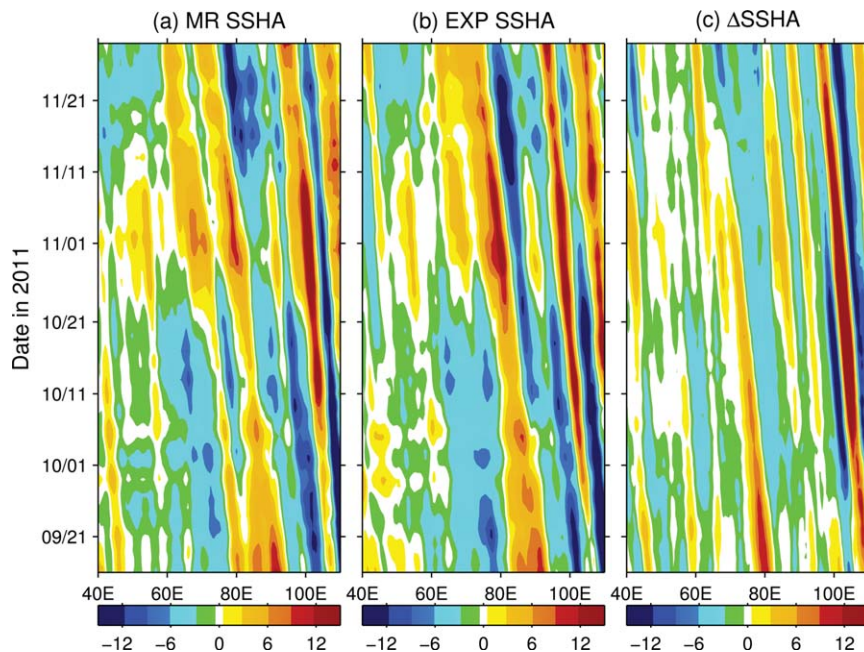
Figure 16. Time-longitude plots of daily SSHA (cm) from (a) MR and (b) EXP, and (c) their difference ΔSSHA averaged in the latitude range of the SCTR (12°–4°S).

shortwave radiation leads to a mean SST warming by about 0.1°C and MLD shoaling by 2–5 m in winter. The diurnal cycle also acts to enhance the 20–90 day SST variability by around 20% in key regions like the SCTR (55°–70°E, 12°–4°S) and the CEIO (65°–95°E, 3°S–3°N). Composite analysis for the wintertime MJO events reveals that at the calm stage of the MJO, under high solar insolation and weak sea surface winds, the diurnal SST variation is strong and induces a 0.1–0.2°C increase in ΔSST. At the wet phase, in contrast, ΔSST is near zero because the diurnal ocean variation is suppressed by strong winds and low insolation. This calm/wet contrast hence amplifies the SST response to the MJO, which is consistent with the mechanism proposed by previous studies for the western Pacific warm pool [*Shinoda and Hendon*, 1998; *Shinoda*, 2005].

[42] The model has also reproduced well the ocean variations associated with two MJO events, MJO 1 and MJO 2, which were monitored by the observation network of the CINDY/DYNAMO field campaign in September-November 2011. During that period, *dSST* magnitude is around 0.7°C in the CEIO due to weak winds and much smaller in the SCTR. MJO 1 exhibits behaviors typical of summertime MJOs, having limited signature in the SCTR. MJO 2, which occurs in November, is initiated in the vicinity of the SCTR and exhibits winter MJO features. During the two events, the diurnal cycle enhances intraseasonal SST changes in both CEIO and SCTR. Different from the wintertime mean situation, in the campaign period the diurnal cycle causes an overall cooling in the SCTR. This is primarily due to the strong easterly trades and deep mean-state MLD. While large wind speed suppresses ocean diurnal variation and its warming rectification on daily mean SST, deep MLD allows nighttime entrainment to bring cold thermocline water into the mixed layer and thereby over-compensates the rectified heating. Besides the effects on intraseasonal SSTA, diurnal ocean variation also modifies

the daily mean Q_T by several W m^{-2} and induces a strong diurnal cycle of it with amplitudes of $O(10$ W m$^{-2})$. Such impact on surface heating have a potential to influence the stability of the low-level atmosphere and trigger convection perturbations associated with MJOs.

References

Antonov, J. I., D. Seidov, T. P. Boyer, R. A. Locarnini, A. V. Mishonov, H. E. Garcia, O. K. Baranova, M. M. Zweng, and D. R. Johnson (2010), *World Ocean Atlas 2009, vol. 2, Salinity*, NOAA Atlas NESDIS 69, edited by S. Levitus, 184 pp., U.S. Gov. Print. Off., Washington, D. C.

Atlas, R., J. Ardizzone, and R. N. Hoffman (2008), Application of satellite surface wind data to ocean wind analysis, *Proc. SPIE*, *7087*, 70870B, doi:10.1117/12.795371.

Bellenger, H., J. P. Duvel, M. Lengaigne, and P. Levan (2009), Impact of organized intraseasonal convective perturbations on the tropical circulation, *Geophys. Res. Lett.*, *36*, L16703, doi:10.1029/2009GL039584.

Bellenger, H., Y. Takayabu, T. Ushiyama, and K. Yoneyama (2010), Role of diurnal warm layers in the diurnal cycle of convection over the tropical Indian Ocean during MISMO, *Mon. Weather Rev.*, *138*, 2426–2433.

Bleck, R. (2002), An oceanic general circulation model framed in hybrid isopycnic-Cartesian coordinates, *Ocean Modell.*, *4*, 55–88.

Bernie, D., S. Woolnough, J. Slingo, and E. Guilyardi (2005), Modeling diurnal and intraseasonal variability of the ocean mixed layer, *J. Clim.*, *18*, 1190–1202.

Bernie, D., E. Guilyardi, G. Madec, J. Slingo, and S. Woolnough (2007), Impact of resolving the diurnal cycle in an atmosphere GCM. Part 1: A diurnally forced OGCM, *Clim. Dyn.*, *29*, 575–590.

Bernie, D., E. Guilyardi, G. Madec, J. Slingo, S. Woolnough, and J. Cole (2008), Impact of resolving the diurnal cycle in an ocean–atmosphere GCM. Part 2: A diurnally coupled CGCM, *Clim. Dyn.*, *31*, 909–925.

Clayson, C. A., and D. Weitlich (2005), Diurnal warming in the tropical Pacific and its interannual variability, *Geophys. Res. Lett.*, *32*, L21604, doi:10.1029/2005GL023786.

Dai, A., and K. E. Trenberth (2004), The diurnal cycle and its depiction in the Community Climate System Model, *J. Clim.*, *17*, 930–951.

Dai, A., T. Qian, K. E. Trenberth, and J. D. Milliman (2009), Changes in continental freshwater discharge from 1948 to 2004, *J. Clim.*, *22*, 2773–2792.

Danabasoglu, G., W. G. Large, J. J. Tribbia, P. R. Gent, B. P. Briegleb, and J. C. McWilliams (2006), Diurnal coupling in the tropical oceans of CCSM3, *J. Clim.*, *19*, 2347–2365.

de Boyer Montégut, C., G. Madec, A. S. Fischer, A. Lazar, and D. Iudicone (2004), Mixed layer depth over the global ocean: An examination of profile data and a profile-based climatology, *J. Geophys. Res.*, *109*, C12003, doi:10.1029/2004JC002378.

Dee, D., S. Uppala, A. Simmons, P. Berrisford, P. Poli, S. Kobayashi, U. Andrae, M. Balmaseda, G. Balsamo, and P. Bauer (2011), The ERA-Interim reanalysis: Configuration and performance of the data assimilation system, *Q. J. R. Meteorol. Soc.*, *137*, 553–597.

Deschamps, P., and R. Frouin (1984), Large diurnal heating of the sea surface observed by the HCMR experiment, *J. Phys. Oceanogr.*, *14*, 177–184.

Duchon, C. E. (1979), Lanczos filtering in one and two dimensions, *J. Appl. Meteorol.*, *18*, 1016–1022.

Duncan, B., and W. Han (2009), Indian Ocean intraseasonal sea surface temperature variability during boreal summer: Madden-Julian Oscillation versus submonthly forcing and processes, *J. Geophys. Res.*, *114*, C05002, doi:10.1029/2008JC004958.

Duvel, J. P., and J. Vialard (2007), Indo-Pacific sea surface temperature perturbations associated with intraseasonal oscillations of tropical convection, *J. Clim.*, *20*, 3056–3082.

Duvel, J. P., R. Roca, and J. Vialard (2004), Ocean mixed layer temperature variations induced by intraseasonal convective perturbations over the Indian Ocean, *J. Atmos. Sci.*, *61*, 1004–1023.

Fairall, C., E. Bradley, J. Godfrey, G. Wick, J. Edson, and G. Young (1996), Cool-skin and warm-layer effects on sea surface temperature, *J. Geophys. Res.*, *101*(C1), 1295–1308.

Fairall, C., E. F. Bradley, J. Hare, A. Grachev, and J. Edson (2003), Bulk parameterization of air-sea fluxes: Updates and verification for the COARE algorithm, *J. Clim.*, *16*, 571–591.

Flament, P., J. Firing, M. Sawyer, and C. Trefois (1994), Amplitude and horizontal structure of a large diurnal sea surface warming event during the Coastal Ocean Dynamics Experiment, *J. Phys. Oceanogr.*, *24*, 124–139.

Flatau, M., P. J. Flatau, P. Phoebus, and P. P. Niiler (1997), The feedback between equatorial convection and local radiative and evaporative processes: The implications for intraseasonal oscillations, *J. Atmos. Sci.*, *54*, 2374–2385.

Gille, S. T. (2012), Diurnal variability of upper ocean temperatures from microwave satellite measurements and Argo profiles, *J. Geophys. Res.*, *117*, C11027, doi:10.1029/2012JC007883.

Girishkumar, M. S., M. Ravichandran, M. J. McPhaden, and R. R. Rao (2011), Intraseasonal variability in barrier layer thickness in the south central Bay of Bengal, *J. Geophys. Res.*, *116*, C03009, doi:10.1029/2010JC006657.

Gregg, M. C., T. B. Sanford, and D. P. Winkel (2003), Reduced mixing from the breaking of internal waves in equatorial waters, *Nature*, *422*(6931), 513–515.

Guemas, V., D. Salas-Mélia, M. Kageyama, H. Giordani, and A. Voldoire (2011), Impact of the ocean mixed layer diurnal variations on the intraseasonal variability of sea surface temperatures in the Atlantic Ocean, *J. Clim.*, *24*, 2889–2914.

Guemas, V., D. Salas-Mélia, M. Kageyama, H. Giordani, and A. Voldoire (2013), Impact of the ocean diurnal cycle on the North Atlantic mean sea surface temperatures in a regionally coupled model, *Dyn. Atmos. Oceans*, *60*, 28–45.

Halliwell, G. R. (2004), Evaluation of vertical coordinate and vertical mixing algorithms in the HYbrid-Coordinate Ocean Model (HYCOM), *Ocean Modell.*, *7*, 285–322.

Halpern, D., and R. K. Reed (1976), Heat budget of the upper ocean under light winds, *J. Phys. Oceanogr.*, *6*, 972–975.

Han, W., and J. P. McCreary (2001), Modeling salinity distributions in the Indian Ocean, *J. Geophys. Res.*, *106*, 859–877.

Han, W., T. Shinoda, L. L. Fu, and J. P. McCreary (2006), Impact of atmospheric intraseasonal oscillations on the Indian Ocean dipole during the 1990s, *J. Phys. Oceanogr.*, *36*, 670–690.

Han, W., D. Yuan, W. T. Liu, and D. Halkides (2007), Intraseasonal variability of Indian Ocean sea surface temperature during boreal winter: Madden-Julian Oscillation versus submonthly forcing and processes, *J. Geophys. Res.*, *112*, C04001, doi:10.1029/2006JC003791.

Han W., P. J. Webster, J. Lin, W. T. Liu and R. Fu, J. Lin and A. Hu (2008), Dynamics of intraseasonal sea level and thermocline variability in the equatorial Atlantic during 2002–2003, *J. Phys. Oceanogr.*, *38*, 945–967.

Harrison, D. E., and G. A. Vecchi (2001), January 1999 Indian Ocean cooling event, *Geophys. Res. Lett.*, *28*, 3717–3720.

Hermes, J. C., and C. J. C. Reason (2008), Annual cycle of the South Indian Ocean (Seychelles–Chagos) thermocline ridge in a regional ocean model, *J. Geophys. Res.*, *113*, C04035, doi:10.1029/2007JC004363.

Hosoda, S., T. Ohira, and T. Nakamura (2008), A monthly mean dataset of global oceanic temperature and salinity derived from Argo float observations, *JAMSTEC Rep. Res. Dev.*, *8*, 47–59.

Inness, P. M., and J. M. Slingo (2003), Simulation of the Madden-Julian oscillation in a coupled general circulation model. Part I: Comparison with observations and an atmosphere-only GCM, *J. Clim.*, *16*(3), 345–364.

Inness, P. M., J. M. Slingo, E. Guilyardi, and J. Cole (2003), Simulation of the Madden-Julian Oscillation in a coupled general circulation model. Part II: The role of the basic state, *J. Clim.*, *16*(3), 365–382.

Izumo, T., S. Masson, J. Vialard, C. de Boyer Montegut, S. K. Behera, G. Madec, K. Takahashi, and T. Yamagata (2010), Low and high frequency Madden–Julian oscillations in austral summer: Interannual variations, *Clim. Dyn.*, *35*, 669–683.

Jayakumar, A., and C. Gnanaseelan (2012), Anomalous intraseasonal events in the thermocline ridge region of Southern Tropical Indian Ocean and their regional impacts, *J. Geophys. Res.*, *117*, C03021, doi:10.1029/2011JC007357.

Jayakumar, A., J. Vialard, M. Lengaigne, C. Gnanaseelan, J. P. McCreary, and B. Praveen Kumar (2011), Processes controlling the surface temperature signature of the Madden–Julian Oscillation in the thermocline ridge of the Indian Ocean, *Clim. Dyn.*, *37*, 2217–2234.

Jerlov, N. G. (1976), *Marine Optics*, Elsevier Sci., Amsterdam.

Jochum, M., and R. Murtugudde (2005), Internal variability of Indian ocean SST, *J. Clim.*, *18*(18), 3726–3738.

Kara, A. B., H. E. Hurlburt, and A. J. Wallcraft (2005), Stability-dependent exchange coefficients for air-sea fluxes, *J. Atmos. Oceanic Technol.*, *22*, 1080–1094.

Kara, A., A. J. Wallcraft, P. J. Martin, and E. P. Chassignet (2008), Performance of mixed layer models in simulating SST in the equatorial Pacific Ocean, *J. Geophys. Res.*, *113*, C02020, doi:10.1029/2007JC004250.

Kawai, Y., and H. Kawamura (2002), Evaluation of the diurnal warming of sea surface temperature using satellite-derived marine meteorological data, *J. Oceanogr.*, *58*, 805–814.

Kawai, Y., and A. Wada (2007), Diurnal sea surface temperature variation and its impact on the atmosphere and ocean: a review, *J. Oceanogr.*, *63*, 721–744.

Kelly, K. A., L. Thompson, W. Cheng, and E. J. Metzger (2007), Evaluation of HYCOM in the Kuroshio extension region using new metrics, *J. Geophys. Res.*, *112*, C01004, doi:10.1029/2006JC003614.

Kennedy, J., P. Brohan, and S. Tett (2007), A global climatology of the diurnal variations in sea-surface temperature and implications for MSU temperature trends, *Geophys. Res. Lett.*, *34*, L05712, doi:10.1029/2006GL028920.

Knutson, T. R., and K. M. Weickmann (1987), 30–60 day atmospheric oscillations: Composite life cycles of convection and circulation anomalies, *Mon. Weather Rev.*, *115*, 1407–1436.

Kummerow, C., W. Barnes, T. Kozu, J. Shiue, and J. Simpson (1998), The Tropical Rainfall Measuring Mission (TRMM) sensor package, *J. Atmos. Oceanic Technol.*, *15*, 809–817.

Large, W. G., J. C. McWilliams, and S. C. Doney (1994), Ocean vertical mixing: A review and a model with a nonlocal boundary layer parameterization, *Rev. Geophys.*, *32*, 363–403, doi:10.1029/94RG01872.

Large, W. G., G. Danabasoglu, S. C. Doney, and J. C. McWilliams (1997), Sensitivity to surface forcing and boundary layer mixing in a global ocean model: Annual-mean climatology, *J. Phys. Oceanogr.*, *27*, 2418–2447.

Lau, W. K., D. E. Waliser, K. Sperber, J. Slingo, and P. Inness (2012), Modeling intraseasonal variability, in *Intraseasonal Variability in the Atmosphere-Ocean Climate System*, edited by W. K. Lau and D. E. Waliser, pp. 399–431, Springer, Berlin.

Liebmann, B., and C. A. Smith (1996), Description of a complete (interpolated), outgoing longwave radiation dataset, *Bull. Am. Meteorol. Soc.*, *77*, 1275–1277.

Lin, J. L., et al. (2006), Tropical intraseasonal variability in 14 IPCC AR4 climate models. Part I: Convective signals, *J. Clim.*, *19*, 2665–2690.

Lloyd, I. D., and G. A. Vecchi (2010), Submonthly Indian Ocean cooling events and their interaction with large-scale conditions, *J. Clim.*, *23*, 700–716.

Locarnini, R. A., A. V. Mishonov, J. I. Antonov, T. P. Boyer, H. E. Garcia, O. K. Baranova, M. M. Zweng, and D. R. Johnson (2010), *World Ocean Atlas 2009, vol. 1, Temperature*, NOAA Atlas NESDIS 68, edited by S. Levitus, 184 pp., U.S. Gov. Print. Off., Washington, D. C.

Loeb, N. G., K. J. Priestley, D. P. Kratz, E. B. Geier, R. N. Green, B. A. Wielicki, P. O. R. Hinton, and S. K. Nolan (2001), Determination of unfiltered radiances from the clouds and the Earth's radiant energy system instrument, *J. Appl. Meteorol.*, *40*, 822–835.

Madden, R. A., and P. R. Julian (1971), Detection of a 40–50 day oscillation in the zonal wind in the tropical Pacific, *J. Atmos. Sci.*, *28*, 702–708.

Masson, S., P. Terray, G. Madec, J.-J. Luo, T. Yamagata, and K. Takahashi (2012), Impact of intra-daily SST variability on ENSO characteristics in a coupled model, *Clim. Dyn.*, *39*, 681–707.

McCreary J. P., P. K. Kundu, and R. L. Molinari (1993), A numerical investigation of dynamics, thermodynamics and mixed layer processes in the Indian Ocean, *Prog. Oceanogr.*, *31*, 181–244.

McCreary, J. P., K. E. Kohler, R. R. Hood, S. Smith, J. Kindle, A. S. Fischer, and R. A. Weller (2001), Influences of diurnal and intraseasonal forcing on mixed-layer and biological variability in the central Arabian Sea, *J. Geophys. Res.*, *106*, 7139–7156.

McPhaden, M. J., et al. (2009), RAMA: The research moored array for African–Asian–Australian monsoon analysis and prediction, *Bull. Am. Meteorol. Soc.*, *90*, 459–480.

Metzger, E., H. Hurlburt, X. Xu, J. F. Shriver, A. Gordon, J. Sprintall, R. Susanto, and H. van Aken (2010), Simulated and observed circulation in the Indonesian Seas: 1/12° global HYCOM and the INSTANT observations, *Dyn. Atmos. Oceans*, *50*, 275–300.

Noh, Y., E. Lee, D.-H. Kim, S.-Y. Hong, M.-J. Kim, and M.-L. Ou (2011), Prediction of the diurnal warming of sea surface temperature using an atmosphere-ocean mixed layer coupled model, *J. Geophys. Res.*, *116*, C11023, doi:10.1029/2011JC006970.

Nyadjro, E. S., B. Subrahmanyam, V. S. N. Murty, and J. F. Shriver (2012), The role of salinity on the dynamics of the Arabian Sea mini warm pool, *J. Geophys. Res.*, *117*, C09002, doi:10.1029/2012JC007978.

Oh, J.-H., B.-M. Kim, K.-Y. Kim, H.-J. Song, and G.-H. Lim (2012), The impact of the diurnal cycle on the MJO over the maritime continent: A modeling study assimilating TRMM rain rate into global analysis, *Clim. Dyn.*, *40*, 893–911.

Papa, F., F. Durand, W. B. Rossow, A. Rahman, and S. K. Bala (2010), Satellite altimeter-derived monthly discharge of the Ganga-Brahmaputra River and its seasonal to interannual variations from 1993 to 2008, *J. Geophys. Res.*, *115*, C12013, doi:10.1029/2009JC006075.

Pimentel, S., K. Haines, and N. Nichols (2008), Modeling the diurnal variability of sea surface temperatures, *J. Geophys. Res.*, *113*, C11004, doi:10.1029/2007JC004607.

Price, J. F., R. A. Weller, and R. Pinkel (1986), Diurnal cycling: Observations and models of the upper ocean response to diurnal heating, cooling, and wind mixing, *J. Geophys. Res.*, *91*(C7), 8411–8427.

Saji, N., S. P. Xie, and C. Y. Tam (2006), Satellite observations of intense intraseasonal cooling events in the tropical south Indian Ocean, *Geophys. Res. Lett.*, *33*, L14704, doi:10.1029/2006GL026525.

Sato, N., C. Takahashi, A. Seiki, K. Yoneyama, R. Shirooka, and Y. Takayabu (2009), An evaluation of the reproducibility of the Madden-Julian oscillation in the CMIP3 multi-models, *J. Meteorol. Soc. Jpn.*, *87*, 791–805.

Saunders, P. M. (1967), The temperature at the ocean-air inter-face, *J. Atmos. Sci.*, *24*, 269–273.

Schiller, A., and J. Godfrey (2003), Indian Ocean intraseasonal variability in an ocean general circulation model, *J. Clim.*, *16*, 21–39.

Schott, F. A., S. P. Xie, and J. P. McCreary Jr (2009), Indian Ocean circulation and climate variability, *Rev. Geophys.*, *47*, RG1002, doi:10.1029/2007RG000245.

Sengupta, D., B. N. Goswami, and R. Senan (2001), Coherent intraseasonal oscillations of ocean and atmosphere during the Asian summer monsoon, *Geophys. Res. Lett.*, *28*, 4127–4130.

Shinoda, T. (2005), Impact of the diurnal cycle of solar radiation on intraseasonal SST variability in the western equatorial Pacific, *J. Clim.*, *18*, 2628–2636.

Shinoda, T., and H. H. Hendon (1998), Mixed layer modeling of intraseasonal variability in the tropical western Pacific and Indian Oceans, *J. Clim.*, *11*, 2668–2685.

Shinoda, T., H. H. Hendon, and J. Glick (1998), Intraseasonal variability of surface fluxes and sea surface temperature in the tropical western Pacific and Indian Oceans, *J. Clim.*, *11*, 1685–1702.

Shinoda, T., W. Han, E. J. Metzger, and H. E. Hurlburt (2012), Seasonal variation of the Indonesian throughflow in Makassar Strait, *J. Phys. Oceanogr.*, *42*, 1099–1123.

Shinoda, T., T. Jensen, M. Flatau, and S. Chen (2013a), Surface wind and upper ocean variability associated with the Madden-Julian Oscillation simulated by the coupled ocean/atmosphere mesoscale prediction system (COAMPS). *Mon. Weather Rev.*, *141*, 2290–2307.

Shinoda, T., T. Jensen, M. Flatau, W. Han, and C. Wang (2013b), Large-scale oceanic variability associated with the Madden-Julian oscillation during the CINDY/DYNAMO field campaign from satellite observations, *Remote Sens.*, *5*, 2072–2092.

Slingo, J., P. Inness, R. Neale, S. Woolnough, and G. Yang (2003), Scale interactions on diurnal to seasonal timescales and their relevanceto model systematic errors, *Ann. Geophys.*, *46*, 139–155.

Smith, W. H. F., and D. T. Sandwell (1997), Global sea floor topography from satellite altimetry and ship depth soundings, *Science*, *277*, 1956–1962.

Soloviev, A., and R. Lukas (1997), Observation of large diurnal warming events in the near-surface layer of the western equatorial Pacific warm pool, *Deep Sea Res. Part I*, *44*, 1055–1076.

Sperber, K. R., S. Gualdi, S. Legutke, and V. Gayler (2005), The Madden–Julian oscillation in ECHAM4 coupled and uncoupled general circulation models, *Clim. Dyn.*, *25*, 117–140.

Stommel, H., K. Saunders, W. Simmons, and J. Cooper (1969), Observations of the diurnal thermocline, *Deep Sea Res.*, *16*, 269–284.

Stramma, L., P. Cornillon, R. A. Weller, J. F. Price, and M. G. Briscoe (1986), Large diurnal sea surface temperature variability: Satellite and in situ measurements, *J. Phys. Oceanogr.*, *16*, 827–837.

Stuart-Menteth, A. C., I. S. Robinson, and P. G. Challenor (2003), A global study of diurnal warming using satellite-derived sea surface temperature, *J. Geophys. Res*, *108*(C5), 3155, doi:10.1029/2002JC001534.

Sverdrup, H. U., R. H. Fleming, and M. W. Johnson (1942), *The Oceans: Their Physics, Chemistry, and General Biology*, Prentice-Hall, New York.

Terray, P., K. Kamala, S. Masson, G. Madec, A. Sahai, J.-J. Luo, and T. Yamagata (2012), The role of the intra-daily SST variability in the Indian monsoon variability and monsoon-ENSO–IOD relationships in a global coupled model, *Clim. Dyn.*, *39*, 729–754.

Thadathil, P., P. M. Muraleedharan, R. R. Rao, Y. K. Somayajulu, G. V. Reddy, and C. Revichandran (2007), Observed seasonal variability of barrier layer in the Bay of Bengal, *J. Geophys. Res.*, *112*, C02009, doi:10.1029/2006JC003651.

Vialard, J., G. Foltz, M. J. McPhaden, J. P. Duvel, and C. de Boyer Montégut (2008), Strong Indian Ocean sea surface temperature signals associated with the Madden-Julian Oscillation in late 2007 and early 2008, *Geophys. Res. Lett.*, *35*, L19608, doi:10.1029/2008GL035238.

Vialard, J., J. Duvel, M. McPhaden, P. Bouruet-Aubertot, B. Ward, E. Key, D. Bourras, R. Weller, P. Minnett, and A. Weill (2009), Cirene: Air-sea interactions in the Seychelles-Chagos thermocline ridge region, *Bull. Am. Meteorol. Soc.*, *90*, 45–61.

Vialard, J., A. Jayakumar, C. Gnanaseelan, M. Lengaigne, D. Sengupta, and B. Goswami (2011), Processes of 30–90 days sea surface temperature variability in the northern Indian Ocean during boreal summer, *Clim. Dyn.*, *38*, 1901–1916.

Vinayachandran, P., and N. Saji (2008), Mechanisms of south Indian Ocean intraseasonal cooling, *Geophys. Res. Lett.*, *35*, L23607, doi:10.1029/2008GL035733.

Vinayachandran, P. N., V. S. N. Murty, and V. Ramesh Babu (2002), Observations of barrier layer formation in the Bay of Bengal during summer monsoon, *J. Geophys. Res.*, *107*(C12), 8018, doi:10.1029/2001JC000831.

Waliser, D. E. (2005), Intraseasonal variability, in *The Asian Monsoon*, edited by B. Wang, p. 844, Springer, Heidelberg.

Waliser, D. E., and N. E. Graham (1993), Convective cloud systems and warm-pool sea surface temperatures: Coupled interactions and self-regulation, *J. Geophys. Res.*, *98*(D7), 12,881–12,893.

Waliser, D. E., K. Lau, and J. H. Kim (1999), The influence of coupled sea surface temperatures on the Madden-Julian oscillation: A model perturbation experiment, *J. Atmos. Sci.*, *56*, 333–358.

Waliser, D. E., R. Murtugudde, and L. E. Lucas (2003), Indo-Pacific Ocean response to atmospheric intraseasonal variability: 1. Austral summer and the Madden-Julian Oscillation, *J. Geophys. Res.*, *108*(C5), 3160, doi:10.1029/2002JC001620.

Waliser, D. E., R. Murtugudde, and L. E. Lucas (2004), Indo-Pacific Ocean response to atmospheric intraseasonal variability: 2. Boreal summer and the intraseasonal oscillation, *J. Geophys. Res.*, *109*, C03030, doi:10.1029/2003JC002002.

Wallcraft, A. J., E. J. Metzger, and S. N. Carroll (2009), Software design description for the HYbrid Coordinate Ocean Model (HYCOM) Version 2.2, Tech. Rep. NRL/MR/7320-09-9166, Nav. Res. Lab., Stennis Space Center, Miss.

Wang, B., and H. Rui (1990), Synoptic climatology of transient tropical intraseasonal convection anomalies: 1975–1985, *Meteorol. Atmos. Phys.*, *44*, 43–61.

Wang, B., and X. S. Xie (1998), Coupled modes of the warm pool climate system. Part 1: The role of air-sea interaction in maintaining Madden-Julian Oscillation, *J. Clim.*, *11*, 2116–2135.

Wang, J.-W., W. Han, and R. L. Sriver (2012a), Impact of tropical cyclones on the ocean heat budget in the Bay of Bengal during 1999: 1. Model configuration and evaluation, *J. Geophys. Res.*, *117*, C09020, doi:10.1029/2012JC008372.

Wang, J.-W., W. Han, and R. L. Sriver (2012b), Impact of tropical cyclones on the ocean heat budget in the Bay of Bengal during 1999: 2. Processes and interpretations, *J. Geophys. Res.*, *117*, C09021, doi:10.1029/2012JC008373.

Watterson, I., and J. Syktus (2007), The influence of air–sea interaction on the Madden–Julian oscillation: The role of the seasonal mean state, *Clim. Dyn.*, *28*, 703–722.

Webber, B. G., A. J. Matthews, K. J. Heywood, and D. P. Stevens (2012), Ocean Rossby waves as a triggering mechanism for primary Madden–Julian events, *Q. J. R. Meteorol. Soc.*, *138*, 514–527.

Webster, P. J., C. A. Clayson, and J. A. Curry (1996), Clouds, radiation, and the diurnal cycle of sea surface temperature in the tropical western pacific, *J. Clim.*, *9*, 1712–1730.

Wentz, F. J., C. Gentemann, D. Smith, and D. Chelton (2000), Satellite measurements of sea surface temperature through clouds, *Science*, *288*, 847–850.

Wheeler M. C., and H. H. Hendon (2004), An all-season real-time multi-variate MJO index: Development of an index for monitoring and prediction, *Mon. Weather Rev.*, *132*, 1917–1932.

Wielicki, B. A., B. R. Barkstrom, E. F. Harrison, R. B. Lee III, G. Louis Smith, and J. E. Cooper (1996), Clouds and the Earth's radiant energy system (CERES): An earth observing system experiment, *Bull. Am. Meteorol. Soc.*, *77*, 853–868.

Woolnough, S. J., J. M. Slingo, and B. J. Hoskins (2000), The relationship between convection and sea surface temperature on intraseasonal time-scales, *J. Clim.*, *13*, 2086–2104.

Woolnough, S. J., J. M. Slingo, and B. J. Hoskins (2001), The organization of tropical convection by intraseasonal sea surface temperature anomalies, *Q. J. R. Meteorol. Soc.*, *127*, 887–907.

Woolnough, S. J., F. Vitart, and M. Balmaseda (2007), The role of the ocean in the Madden–Julian Oscillation: Implications for MJO prediction, *Q. J. R. Meteorol. Soc.*, *133*, 117–128.

Xavier, P. K. (2012), Intraseasonal convective moistening in CMIP3 models, *J. Clim.*, *25*, 2569–2577.

Xie, S.-P., H. Annamalai, F. A. Schott, and J. P. McCreary Jr (2002), Structure and mechanisms of south Indian Ocean climate variability, *J. Clim.*, *15*, 864–878.

Yang, G.-Y., and J. Slingo (2001), The diurnal cycle in the tropics, *Mon. Weather Rev.*, *129*, 784–801.

Yang, J., Q. Bao, X. Wang, and T. Zhou (2012), The tropical intraseasonal oscillation in SAMIL coupled and uncoupled general circulation models, *Adv. Atmos. Sci.*, *29*, 529–543.

Yokoyama, R., S. Tanba, and T. Souma (1995), Sea surface effects on the sea surface temperature estimation by remote sensing, *Remote Sens.*, *16*, 227–238.

Yoneyama, K., C. Zhang, and C. N. Long (2013), Tracking pulses of the Madden-Julian oscillation, *Bull. Amer. Meteorol. Soc.*, doi:http://dx.doi.org/10.1175/BAMS-D-12–00157.1, in press.

Yuan, D., and W. Han (2006), Roles of equatorial waves and western boundary reflection in the seasonal circulation of the equatorial Indian Ocean, *J. Phys. Oceanogr.*, *36*, 930–944.

Zhang, C. (2005), Madden-Julian Oscillation, *Rev. Geophys.*, *43*, RG2003, doi:10.1029/2004RG000158.

Zhang, C., and M. Dong (2004), Seasonality in the Madden-Julian oscillation, *J. Clim.*, *17*, 3169–3180.

Zhang, C., M. Dong, S. Gualdi, H. H. Hendon, E. D. Maloney, A. Marshall, K. R. Sperber, and W. Wang (2006), Simulations of the Madden–Julian oscillation in four pairs of coupled and uncoupled models, *Clim. Dyn.*, *27*, 573–592.

Zhang, C., J. Gottschalck, E. D. Maloney, M. W. Moncrieff, F. Vitart, D. E. Waliser, B. Wang, and M. C. Wheeler (2013), Cracking the MJO nut, *Geophys. Res. Lett.*, *40*, 1223–1230, doi:10.1002/grl.50244.

Zhang, X., Y. Lu, K. R. Thompson, J. Jiang, and H. Ritchie (2010), Tropical Pacific Ocean and the Madden-Julian Oscillation: Role of wind and buoyancy forcing, *J. Geophys. Res.*, *115*, C05022, doi:10.1029/2009JC005734.

Zhao, C., T. Li, and T. Zhou (2013), Precursor signals and processes associated with MJO initiation over the tropical Indian Ocean, *J. Clim.*, *26*, 291–307.

Zhou, L., R. Murtugudde, and M. Jochum (2008), Dynamics of the intra-seasonal oscillations in the Indian Ocean south equatorial current, *J. Phys. Oceanogr.*, *38*, 121–132.